Probing low scale leptogenesis through gravitational wave

Anirban Biswas[1,*] and Sougata Ganguly[2,†]

[1]Department of Physics, Gaya College (a constituent unit of Magadh University, Bodh Gaya), Gaya 823001, India
[2]Particle Theory and Cosmology Group, Center for Theoretical Physics of the Universe, Institute for Basic Science (IBS), Daejeon, 34126, Korea

(Received 13 May 2025; accepted 28 January 2026; published 24 February 2026)

The quest for a common origin of neutrino mass and baryogenesis is one of the long-standing goals in particle physics. A minimal gauge extension of the Standard Model by $U(1)_{\mathrm{B-L}}$ symmetry provides a unique scenario to explain the tiny mass of neutrinos as well as the observed baryon asymmetry, both by virtue of three right-handed neutrinos (RHNs). Additionally, the $U(1)_{\mathrm{B-L}}$ breaking scalar that generates mass of the RHNs can produce a stochastic gravitational wave background (SGWB) via cosmological first-order phase transition. In this work, we systematically investigate TeV-scale leptogenesis considering flavor effects that are crucial in the low-temperature regime. We also explore all possible RHN production channels, which can have significant impact on the abundance of RHNs, depending on the value of the $U(1)_{\mathrm{B-L}}$ gauge coupling. We demonstrate that the strong dependence of the $U(1)_{\mathrm{B-L}}$ gauge sector on the baryon asymmetry as well as SGWB production can be utilized to probe a region of the model parameter space. In particular, we find that a $U(1)_{\mathrm{B-L}}$ gauge boson with mass $\sim$10 TeV and gauge coupling $\sim$0.1 can explain the observed baryon asymmetry and produces a detectable SGWB in future detectors as well. Importantly, this region falls beyond the reach of the current collider sensitivity.

DOI: 10.1103/zkrc-lrs5

I. INTRODUCTION

The Standard Model (SM) of particle physics is an extremely successful theory in order to explain the observable phenomena below the TeV scale. Despite its tremendous successes, the observation of neutrino oscillation [1,2] raises a fundamental question about the completeness of the SM since neutrinos are massless in the SM. Neutrino oscillation predicts that the neutrinos have a very tiny mass, typically in the ballpark of 0.1 eV. There are many beyond the Standard Model (BSM) frameworks that explain the neutrino masses and their mixings. However, the SM augmented with at least two heavy right-handed neutrinos (RHNs) is the simplest BSM scenario in order to explain the tininess of the neutrino mass as well as the neutrino oscillation parameters, and it is known as the "type-I seesaw" mechanism [3,4].

Another important shortcoming of the SM is its inability to explain the observed baryon asymmetry of the Universe. The observation of the cosmic microwave background (CMB) by the *Planck* satellite and the prediction of big bang nucleosynthesis strongly suggest an excess of the baryon over the antibaryon, and it is quantified as the baryon-to-photon ratio η_B. The current value of η_B is $(6.143 \pm 0.190) \times 10^{-10}$ [5]. The explanation of η requires charge-parity (CP) violation in the theory. In the SM, CP violation exists in the quark sector, but the amount of CP violation [$\mathcal{O}(10^{-20})$] is way smaller than the value required to explain the CMB prediction of η_B [6].

In light of the baryon asymmetric universe, many baryogenesis mechanisms have been proposed [7–15]. Among them, the production of baryon asymmetry from the asymmetry in the leptonic sector known as "leptogenesis" is a very well-studied scenario [6,16–33]. In the SM, the baryon number B and the lepton number L are not good quantum numbers since they are not conserved at the quantum level. However, B − L is a good quantum number. The basic principle of leptogenesis is to convert the asymmetry in the leptonic sector to the asymmetry in the baryonic sector via the B − L conserving sphaleron process, which is active when the temperature of the Universe (T) lies between $\sim$130 and 10^{12} GeV. Thus, asymmetry in the leptonic sector produced in the temperature range between 130 and 10^{12} GeV can be efficiently converted into baryon asymmetry thanks to B − L conserving and B + L violating the electroweak sphaleron process.

The production of baryon asymmetry via leptogenesis is a natural consequence of the type-I seesaw framework. In

*Contact author: anirban.biswas.sinp@gmail.com
†Contact author: sganguly0205@ibs.re.kr

Published by the American Physical Society under the terms of the Creative Commons Attribution 4.0 International license. Further distribution of this work must maintain attribution to the author(s) and the published article's title, journal citation, and DOI. Funded by SCOAP³.

this framework, CP violation in the leptonic sector is sourced by the complex Yukawa couplings between the heavy RHNs and the SM sectors. In the presence of complex Yukawa couplings, the decay of heavy RHNs into SM leptons and the Higgs doublet generates the CP asymmetry. Under the assumption that the heavy RHNs with the hierarchical mass spectrum are in thermal equilibrium in the early Universe, the lepton asymmetry generated by the lightest RHN only survives. In this vanilla leptogenesis scenario, the mass of the RHN is required to be larger than 10^9 GeV, known as the Davidson-Ibarra bound [34], in order to explain the baryon asymmetry.

The minimum mass required in this scenario is much larger than the current reach of collider experiments. The resonant leptogenesis is an interesting possibility to lower the minimum mass of the RHN to approximately the TeV scale. In this mechanism, the key idea is that if the two RHNs have a nearly degenerate mass spectrum, the leptonic asymmetry will be resonantly enhanced and generate the correct baryon asymmetry via leptogenesis, even if the mass of the RHNs is in the TeV scale. However, another important aspect of low scale leptogenesis is the flavor effects. When the temperature of the Universe is higher than 10^{12} GeV, the Yukawa interactions of the SM leptons are out of equilibrium, making different lepton flavors indistinguishable. However, as the temperature becomes smaller than 10^{12} GeV, the Yukawa interaction involving a tau lepton enters the equilibrium. As a result, for 10^9 GeV $\lesssim T \lesssim 10^{12}$ GeV, the tau flavor can be discriminated from the other two flavors. Moreover, for $T \lesssim 10^9$ GeV, the Yukawa interaction of the second-generation leptons also enters the equilibrium, and muon flavor is also distinguishable. Finally, when the temperature $T \lesssim 10^5$ GeV, all three flavors are in thermal equilibrium through Yukawa interactions, and we need to consider their effects in the lepton asymmetry calculation separately, as discussed in [35–40].

Baryon asymmetry produced via leptogenesis requires a new physics at a scale much larger than the electroweak scale. The detection of the stochastic gravitational wave background (SGWB) in future gravitational wave (GW) detectors can be used to probe these kinds of high scale theories. The SGWB in the early Universe can originate from cosmic strings [41–44], quantum fluctuations during reheating [45,46], first-order phase transitions [47,48], etc. (see [49] for more details). BSM models with an extended scalar sector are an obvious source of SGWB production in the early Universe via a first-order phase transition (FOPT), and it has been extensively studied in various BSM models, as discussed in [50–76]. Other cosmological and phenomenological consequences of an FOPT, such as dark matter production, the generation of baryon asymmetry, and the formation of a primordial black hole, have been discussed in [77–87].

The detection of the SGWB in future GW detectors has also been investigated in the context of probing the seesaw scale [80–82,88–93]. In this work, we consider a gauged $U(1)_{\mathrm{B-L}}$ extension of the SM with three heavy RHNs (N_i, $i = 1, \ldots, 3$) with B − L charge -1 and a complex scalar Φ which carries B − L charge $+2$. The former fields are required to satisfy the anomaly-free conditions, whereas the latter field is required to break the $U(1)_{\mathrm{B-L}}$ symmetry and generate the mass of the heavy RHNs. Thus, in this framework, one can dynamically generate the heavy mass of the RHNs once Φ acquires a nonzero vacuum expectation value (VEV). Here, we have studied the production of baryon asymmetry from the decay of TeV scale RHNs. We would like to mention that our model is different from the one considered in Refs. [81,82] where the authors have studied leptogenesis and an FOPT in a scale invariant $B - L$ model. Because of the scale invariance, the predicted strength of the GW is different from that obtained in our study. Additionally, in our analysis, we have considered (i) the flavor effects, which are important for such a low scale leptogenesis scenario, and (ii) the effect of the B − L gauge boson Z_{BL} and Φ involving RHNs production channels. We find that the parameters of the $U(1)_{\mathrm{B-L}}$ gauge sector as well as the Yukawa interaction strength between Φ and N_i have strong dependence on the baryon asymmetry generation.

In addition, the scalar sector augmented with an extra scalar Φ can undergo an FOPT in the early Universe and produces an SGWB. Since the masses of the RHNs and Z_{BL} depend on the B − L breaking scale, the SGWB production also depends on the parameters of the $U(1)_{\mathrm{B-L}}$ gauge sector. In light of this interconnection between the production of baryon asymmetry and the SGWB from an FOPT, we investigate the possibility of probing the parameter space for leptogenesis in future GW detectors such as LISA [94], BBO [95–97], DECIGO, and Ultimate DECIGO (U-DECIGO) [98–100]. We show the region of model parameter space where the observed baryon asymmetry can be explained via resonant flavored leptogenesis. Interestingly, a certain portion of this parameter space is capable of producing a detectable SGWB in future detectors. We also discuss the current collider constraints on our model parameters.

The rest of the paper is organized as follows: We briefly discuss our model in Sec. II. The constraints on the model parameter space are discussed in Sec. III. A detailed discussion on resonant flavored leptogenesis is given in Sec. IV. Section V is devoted to a detailed discussion on FOPT dynamics, GW production from an FOPT, and the prospects of detecting an SGWB in future GW detectors. Finally, we conclude in Sec. VI. The derivation of the $\mathcal{A}$ matrix for flavored leptogenesis is given in Appendix A. In Appendix B, all the relevant cross sections for the analysis of resonant flavored leptogenesis are given. In Appendix C, we provide the explicit forms of the collision terms for a few

lepton-number-violating processes. The field-dependent and thermal masses of all the fields are given in Appendix D.

II. MODEL

In this section, we will describe our model briefly. We extend the SM gauge group $SU(3)_c \otimes SU(2)_L \otimes U(1)_Y$ with an additional $U(1)_{\mathrm{B-L}}$ gauge symmetry. We introduce three RHNs N_i (where $i = 1, 2, 3$) with B − L charge −1 in order to make the model anomaly-free. To break the $U(1)_{\mathrm{B-L}}$ gauge symmetry and generate the mass of the RHN, a complex scalar Φ with B − L charge +2 has been introduced.

The Lagrangian of the model is given by

$$\mathcal{L} = \mathcal{L}^{\mathrm{SM}}_{\mathrm{Gauge}} + \mathcal{L}^{\mathrm{SM}}_{\mathrm{Yukawa}} + \mathcal{L}_{\mathrm{New}} + V(H, \Phi), \tag{1}$$

where $\mathcal{L}^{\mathrm{SM}}_{\mathrm{Gauge}}$ and $\mathcal{L}^{\mathrm{SM}}_{\mathrm{Yukawa}}$ are the Lagrangians for the SM gauge and Yukawa interactions, respectively. $V(H, \Phi)$ is the scalar potential, and it reads

$$V(H,\Phi) = -\mu_H^2 H^\dagger H - \mu_\Phi^2 \Phi^\dagger\Phi + \lambda_H (H^\dagger H)^2 + \lambda_\phi (\Phi^\dagger\Phi)^2 - \lambda' H^\dagger H \Phi^\dagger \Phi, \tag{2}$$

where μ_H and μ_Φ are mass parameters of H and Φ, respectively, and the quartic couplings of H and Φ are denoted by λ_H and λ_ϕ, respectively. The explicit forms of H and Φ are given by

$$H = \begin{pmatrix} G^+ \\ \frac{\zeta_1 + i\zeta_2}{\sqrt{2}} \end{pmatrix}, \qquad \Phi = \frac{\eta_1 + i\eta_2}{\sqrt{2}}, \tag{3}$$

and at zero temperature, ζ_1 and η_1 acquire nonzero VEVs v_h and v_{BL}, respectively. The last term of Eq. (2) is the mixing between the SM Higgs boson and $U(1)_{\mathrm{B-L}}$ symmetry-breaking scalar, and it is proportional to the coupling λ'. The parameters in Eq. (2) can be written in terms of the masses and mixing angle between scalars, as follows:

$$\begin{aligned}
\mu_H^2 &= \frac{(m_\eta^2 + m_\zeta^2) v_h - (m_\eta^2 - m_\zeta^2)(v_h \cos 2\theta + v_{\mathrm{BL}} \sin 2\theta)}{4 v_h}, \\
\mu_\Phi^2 &= \frac{(m_\eta^2 + m_\zeta^2) v_{\mathrm{BL}} + (m_\eta^2 - m_\zeta^2)(v_{\mathrm{BL}} \cos 2\theta - v_h \sin 2\theta)}{4 v_{\mathrm{BL}}}, \\
\lambda_H &= \frac{m_\eta^2 + m_\zeta^2 - (m_\eta^2 - m_\zeta^2)\cos 2\theta}{4 v_h^2}, \\
\lambda_\Phi &= \frac{m_\eta^2 + m_\zeta^2 + (m_\eta^2 - m_\zeta^2)\cos 2\theta}{4 v_{\mathrm{BL}}^2}, \\
\lambda' &= -\frac{(m_\zeta^2 - m_\eta^2)\sin\theta\cos\theta}{v_h v_{\mathrm{BL}}},
\end{aligned} \tag{4}$$

where η and ζ are the two scalar degrees of freedom in the mass basis with masses m_η and m_ζ, respectively. In the limit $\theta \to 0$, $m_\zeta^2 \to 2\lambda_H v_h^2$, and thus ζ is identified as an SM Higgs boson.

The interactions of the SM fields with a B − L gauge boson Z_{BL}, Φ as well as the kinetic terms of Z_{BL}, Φ, and N_i are contained in $\mathcal{L}_{\mathrm{New}}$, and it can be written as

$$\begin{aligned}
\mathcal{L}_{\mathrm{New}} = &-\frac{1}{4} X^{\mu\nu} X_{\mu\nu} + \sum_{i=1}^{3} i\overline{N_{iR}} \not{D} N_{iR} \\
&- \sum_{i=1}^{3} \left(\frac{Y_i}{2} \overline{N^c_{i_R}} N_{i_R} \Phi + \mathrm{H.c} \right) - g_{\mathrm{BL}} \sum_{f \neq \nu} Q^{(f)}_{\mathrm{BL}} \bar{f} \gamma_\mu f Z^\mu_{\mathrm{BL}} \\
&- g_{\mathrm{BL}} \sum_{i=1}^{3} Q^{(\nu)}_{\mathrm{BL}} \bar{\nu}_i \gamma_\mu P_L \nu_i Z^\mu_{\mathrm{BL}} - \sum_{\alpha,i} Y_{D\alpha i} \overline{L_\alpha} \tilde{H} N_{iR},
\end{aligned} \tag{5}$$

where f is the charged SM fermion, and ν_i ($i = 1, 2, 3$) is the SM neutrino. $Q^{(f)}_{\mathrm{BL}}$ and $Q^{(\nu)}_{\mathrm{BL}}$ are the B − L charges of the charged SM fermions and SM neutrinos, respectively. $Q^{(f)}_{\mathrm{BL}} = -1(1/3)$ for the charged SM leptons (quarks) and $Q^{(\nu)}_{\mathrm{BL}} = -1$ for the SM neutrinos. The $U(1)_{\mathrm{B-L}}$ gauge coupling is denoted by g_{BL}, and $X^{\mu\nu} = \partial^\mu Z^\nu_{\mathrm{BL}} - \partial^\nu Z^\mu_{\mathrm{BL}}$ is the field strength tensor of the B − L gauge boson Z_{BL}. In the present scenario, we have not considered kinetic mixing between $U(1)_{\mathrm{B-L}}$ and $U(1)_{\mathrm{Y}}$. This assumption can be justified because introducing kinetic mixing does not reveal any new physics since the SM fermions are already coupled to Z_{BL} due to their nonzero B − L charge. Therefore, the effect of $Z - Z_{\mathrm{BL}}$ mixing on top of the tree-level interaction can be safely neglected. The Yukawa coupling coefficient between N_i and Φ is denoted by Y_i. The last term is the Dirac-Yukawa interaction among the lepton doublet, the Higgs doublet, and the RHN. This interaction is responsible for the Dirac mass of the neutrinos, similar to the other charged fermions in the SM. Moreover, the lepton asymmetry generated from the out-of-equilibrium decay of RHNs is also due to the Dirac-Yukawa interaction. In the present scenario, we have used the Casas-Ibarra parametrization [101] to calculate the Dirac-Yukawa coupling matrix Y_D. According to this formalism, we can express Y_D as

$$Y_D = M^{1/2} R D_\nu^{1/2} U^\dagger, \tag{6}$$

where M, D_ν are the RHN and light neutrino mass matrices, respectively, and they are assumed to be diagonal. The matrix U is the Pontecorvo-Maki-Nakagawa-Sakata matrix, and R is an orthogonal matrix with complex parameters. In this work, we take a simple form of R as

$$R = \begin{pmatrix} 0 & \cos\Theta & \sin\Theta \\ 0 & -\sin\Theta & \cos\Theta \\ 1 & 0 & 0 \end{pmatrix}, \tag{7}$$

with $\Theta = \theta_R + i\theta_I$, and the explicit values of θ_R and θ_I will be discussed in the next section. The particular form of R ensures that the Yukawa coupling matrix Y_D is independent of M_3 when the lightest active neutrino mass is chosen to be zero, i.e., $m_1 = 0$ [102]. Moreover, in this formalism, the Yukawa couplings (Y_{D3i}, $i = 1, 2, 3$) associated with the third generation of the SM leptons are zero. As a result, no CP asymmetry is generated for the third generation from the decays of RHNs.

The $U(1)_{B-L}$ symmetry is spontaneously broken when the scalar Φ gets a VEV, and as a result the $B - L$ gauge boson and the RHNs become massive. Therefore, after symmetry breaking, the masses of Z_{BL} and N_is are given by

$$m_{Z_{BL}} = 2g_{BL}v_{BL}, \tag{8}$$

$$M_i = Y_i \frac{v_{BL}}{\sqrt{2}}. \tag{9}$$

We will see in Sec. IV that for successful low scale leptogenesis, we require the lightest two RHNs to be quasidegenerate, i.e., $Y_1 \approx Y_2$, while the mass gaps between N_3, and $N_{1,2}$ are much larger than the decay widths of $N_{1,2}$, so that the asymmetry generated from N_3 is not resonantly enhanced. In our analysis, we have considered $Y_3 \gg Y_1, Y_2$ so that $M_3 \gg M_1, M_2$. The choice of this mass hierarchy implies that the lepton asymmetry is produced only from the decays of N_1 and N_2, and at the time of asymmetry generation, the abundance of N_3 is Boltzmann suppressed.

III. RELEVANT CONSTRAINTS

A. Constraint from electroweak precision observables (EWPO)

The new physics effect on the EWPO observables can be parametrized by the oblique parameters S, T, and U [103]. In our scenario, the self-energy correction of ZZ and W^+W^- gets an additional contribution due to the mixing between Φ and the Higss field, and as a result, the oblique parameters are modified. The change in the oblique parameters in the presence of a new scalar field is given by

$$\begin{aligned}
\Delta T &= \frac{3}{16\pi \sin^2\theta_W}\left[\cos^2\theta\left\{f_T\left(\frac{m_\zeta^2}{m_W^2}\right) - \frac{1}{\cos^2\theta_W^2} f_T\left(\frac{m_\zeta^2}{m_Z^2}\right)\right\} + \sin^2\theta\left\{f_T\left(\frac{m_\eta^2}{m_W^2}\right) - \frac{1}{\cos^2\theta_W^2} f_T\left(\frac{m_\eta^2}{m_Z^2}\right)\right\}\right. \\
&\quad \left. - \left\{f_T\left(\frac{m_\zeta^2}{m_W^2}\right) - \frac{1}{\cos^2\theta_W^2} f_T\left(\frac{m_\zeta^2}{m_Z^2}\right)\right\}\right], \\
\Delta S &= \frac{1}{2\pi}\left[\cos^2\theta f_S\left(\frac{m_\zeta^2}{m_Z^2}\right) + \sin^2\theta f_S\left(\frac{m_\eta^2}{m_Z^2}\right) - f_S\left(\frac{m_\zeta^2}{m_Z^2}\right)\right], \\
\Delta U &= \frac{1}{2\pi}\left[\cos^2\theta f_S\left(\frac{m_\zeta^2}{m_W^2}\right) + \sin^2\theta f_S\left(\frac{m_\eta^2}{m_W^2}\right) - f_S\left(\frac{m_\zeta^2}{m_W^2}\right)\right] - \Delta S,
\end{aligned} \tag{10}$$

where θ_W is the Weinberg angle, $\sin^2\theta_W = 0.231$, and $m_\zeta = 125$ GeV [5]. The loop functions $f_T(x)$ and $f_S(x)$ are given by [104]

$$\begin{aligned}
f_T(x) &= \frac{x\log x}{x-1}, \\
&\underline{\text{for } 0 < x < 4:} \\
f_S(x) &= \frac{1}{12}\left[-2x^2 + 9x + \{(x-3)(x^2-4x+12) + \frac{1-x}{x}\} f_T(x) + \sqrt{x(4-x)}(x^2-4x+12)\tan^{-1}\left(\sqrt{\frac{4-x}{x}}\right)\right], \\
&\underline{\text{for } x \geq 4:} \\
f_S(x) &= \frac{1}{12}\left[-2x^2 + 9x + \left\{(x-3)(x^2-4x+12) + \frac{1-x}{x}\right\} f_T(x) + \sqrt{x(x-4)}(x^2-4x+12)\right. \\
&\quad \left. \times \log\left(\frac{x - \sqrt{x(x-4)}}{x + \sqrt{x(x-4)}}\right)\right].
\end{aligned} \tag{11}$$

To derive the constraint from the EWPO, we use $\Delta S = 0.04 \pm 0.11$, $\Delta T = 0.09 \pm 0.14$, and $\Delta U = -0.02 \pm 0.11$ and following [56,58], we define $\Delta\chi^2$ as

$$\Delta\chi^2 = \sum_{i,j}(\Delta\mathcal{O}_i - \Delta\mathcal{O}_{\mathrm{obs},i})[\mathcal{C}^{-1}]_{ij}(\Delta\mathcal{O}_j - \Delta\mathcal{O}_{\mathrm{obs},j}),$$

where

$$\Delta\mathcal{O} = (\Delta S \Delta T \Delta U)^T, \qquad \Delta\mathcal{O}_{\mathrm{obs}} = (0.04\, 0.09 - 0.02)^T.$$

The ij element of the covariance matrix $\mathcal{C}$ is $\sigma_i\rho_{ij}\sigma_j$, and the explicit forms of σ and ρ are given by

$$\sigma = (\,0.11 \quad 0.14 \quad 0.11\,)^T,$$
$$\rho = \begin{pmatrix} 1 & 0.92 & -068 \\ 0.92 & 1 & -0.87 \\ -0.68 & -0.87 & 1 \end{pmatrix}. \tag{12}$$

We determine the allowed model parameters at 95% confidence interval by imposing the condition $\Delta\chi^2 < 5.99$.

B. Higgs signal strength

The mixing angle between the scalar fields can be constrained from the measurement of the Higgs signal strength at the LHC. Combining the constraints in different channels, the current bound on the Higgs signal strength (r_h) is $1.02^{+0.11}_{-0.12}$, which reflects the absence of any deviation from the SM prediction [105]. The signal strength r_h in any channel XX is defined as [106]

$$r_h = \frac{\sigma_{gg\to\zeta}\mathrm{Br}(\zeta\to XX)}{\sigma^{\mathrm{SM}}_{gg\to h}\mathrm{Br}(h\to XX)_{\mathrm{SM}}} = \cos^2\theta\times\cos^2\theta\times\frac{\Gamma^{\mathrm{SM}}_h}{\Gamma_\zeta}, \tag{13}$$

where $\Gamma^{\mathrm{SM}}_h = 3.7$ MeV is the total decay width of the SM Higgs boson [5]. $\Gamma_\zeta = \cos^2\theta\Gamma^{\mathrm{SM}}_h + \sum_i \Gamma_{\zeta\to N_iN_i}\Theta(m_\zeta - 2M_i) + \Gamma_{\zeta\to\eta\eta}\Theta(m_\zeta - 2m_\eta)$. In our parameter space of interest, $\Gamma_{\zeta\to N_iN_i} = \Gamma_{\zeta\to\eta\eta} = 0$ and the Higgs signal strength bound can be translated into the bound on the mixing angle as $\sin^2\theta \le 0.22$ at 95% CL.

C. LEP and LHC constraint on Z_{BL}

The measurement of $e^+e^-\to\ell^+\ell^-$ at the LEP constrains the $m_{Z_{\mathrm{BL}}} - g_{\mathrm{BL}}$ plane as $m_{Z_{\mathrm{BL}}}/g_{\mathrm{BL}} > 6$ TeV [107]. However, for $m_{Z_{\mathrm{BL}}} < 5$ TeV, the bound from the dilepton search at the LHC is stronger than the LEP constraint [108].

IV. FLAVORED LEPTOGENESIS

The out-of-equilibrium decays of RHNs into the SM lepton and scalar can generate an asymmetry between the particle and antiparticle in the leptonic sector if there are some lepton-number-violating interactions and simultaneous C and CP violations as well. The lepton asymmetry thus generated is efficiently converted into the baryon asymmetry by the B − L conserving sphaleron processes as long as the sphalerons are in thermal equilibrium with the SM plasma ($T \gtrsim 130$ GeV). In the present scenario, we consider the masses of the RHNs and Z_{BL} are of the order of TeV scale to test this model in future GW detectors, as discussed in Sec. V, and this can be achieved by choosing v_{BL}, g_{BL}, and Y_i appropriately. This restriction automatically implies that the masses of the RHNs generated through the spontaneous breaking of $U(1)_{\mathrm{B-L}}$ symmetry would be much smaller than the canonical mass scale of the RHN ($\gtrsim 10^9$ GeV) required for the vanilla leptogenesis scenario. Therefore, the leptogenesis occurs at a much lower temperature, and in this case, the flavor effect becomes important. The main reason is that when the temperature is above 10^{12} GeV, we do not need to consider three lepton flavor states separately, instead they can be considered as a coherent superposition of all three flavor states (e, μ, and τ). However, the coherence is lost due to the Yukawa interaction which becomes effective at different temperatures for different flavors. Consequently, we have three distinct regimes, namely, the unflavored regime, partly flavored regime, and fully flavored regime, respectively. The unflavored regime refers to an era when $T \gtrsim 10^{12}$ GeV. When the temperature drops below 10^{12} GeV, the Yukawa interaction of the τ lepton becomes larger than the corresponding Hubble expansion rate, and the coherence between τ and the other two flavors (e and μ) is lost. This is known as a partly flavored regime since in this regime, one needs to consider the τ lepton separately while e and μ still maintain coherence. This situation continues until the temperature drops below 10^9 GeV when the Yukawa interaction of the muon enters equilibrium, and all three flavors now become distinctly different. This is known as the fully flavored regime. As mentioned above, the mass scale of the RHNs is a few TeV; therefore, we are essentially working in the fully flavored regime where lepton asymmetry for all three flavors needs to be computed separately by solving individual Boltzmann equations. Moreover, at this low energy scale $T \sim M_1$ (M_1 is the mass of the lightest RHN), as the desired lepton asymmetry cannot be generated through vanilla leptogenesis, we need some mechanism to enhance the CP asymmetry. This can be achieved due to a resonant enhancement in the CP asymmetry parameter if we have two quasidegenerate RHNs. The resonant leptogenesis is immensely popular from the point of view of the detection prospect of the RHN states in ongoing experiments, particularly at the LHC, which is capable of producing TeV scale particles from pp collisions [109,110].

Let us consider $Y_{\ell_{L_\alpha}}$ as the coming number density of the lepton doublet of flavor α, which is defined as $Y_{\ell_{L_\alpha}} = n_{\ell_{L_\alpha}}/s$ where $n_{\ell_{L_\alpha}}$ is the number density of flavor α, and s is the entropy density. Now, we define the comoving number density for the lepton asymmetry of flavor α as

$\Delta Y_{\ell_{L_\alpha}} = Y_{\ell_{L_\alpha}} - Y_{\overline{\ell}_{L_\alpha}}$. However, $\Delta Y_{\ell_{L_\alpha}}$ is not a conserved quantity since in the SM, the lepton number is violated by the sphaleron processes. Thus, we would like to calculate $\Delta B/3 - \Delta L_\alpha$, which is conserved by the sphaleron processes, and L_α is the total lepton number of flavor α. Therefore, $\Delta Y_{\ell_{L_\alpha}}$ generated through the decays of the RHNs is redistributed to the $B/3 - L_\alpha$ asymmetry via the $B/3 - L_\alpha$ conserving sphaleron processes, and it can be expressed as

$$\Delta Y_{\ell_{L_\alpha}} = -\sum_{\beta=e,\mu,\tau} \mathcal{A}_{\alpha\beta}\, Y_{\Delta_\beta}, \tag{14}$$

where $\Delta_\alpha \equiv \Delta B/3 - \Delta L_\alpha$, and the $\mathcal{A}$ matrix when all the SM Yukawa couplings are in equilibrium (when $T \leq 10^5$ GeV) is given by [111]

$$\mathcal{A} = \frac{1}{711}\begin{pmatrix} 442 & -32 & -32 \\ -32 & 442 & -32 \\ -32 & -32 & 442 \end{pmatrix}. \tag{15}$$

It is a symmetric matrix with $\mathcal{O}(1)$ diagonal elements and tiny off-diagonal elements. The baryon asymmetry ΔY_B is related to Y_{Δ_α} by the sphaleron factor $28/79$ as

$$\Delta Y_B = \frac{28}{79}\sum_\alpha Y_{\Delta_\alpha}. \tag{16}$$

The derivation of the $\mathcal{A}$ matrix and the sphaleron factor is given in Appendix A.

Finally, ΔY_B is related to the baryon-to-photon ratio of the Universe as

$$\eta_B = \frac{\Delta Y_B s}{n_\gamma}, \tag{17}$$

$$= 7.0397 \Delta Y_B, \tag{18}$$

where $n_\gamma = 410.7\ \text{cm}^{-3}$ and $s = 2891.2\ \text{cm}^{-3}$ are the number density of the photon and the entropy density of the Universe at the present epoch, respectively. The current value of the baryon-to-photon ratio is $\eta_B = (6.143 \pm 0.190) \times 10^{-10}$ [5].

Keeping in mind the above discussion, we will now write the Boltzmann equations for the comoving number densities of the RHNs and Δ_α, respectively,

$$\begin{aligned}\frac{dY_{N_i}}{dz} = -\frac{1}{zH}\Bigg[&\langle\Gamma_i\rangle(Y_{N_i} - Y_{N_i}^{\text{eq}}) \\ &- \langle\Gamma_{Z_{\text{BL}}\to N_i N_i}\rangle Y_{Z_{\text{BL}}}^{\text{eq}}\left(1 - \left(\frac{Y_{N_i}}{Y_{N_i}^{\text{eq}}}\right)^2\right) \\ &+ \frac{\gamma_{\text{tot}}}{s}\left(\left(\frac{Y_{N_i}}{Y_{N_i}^{\text{eq}}}\right)^2 - 1\right) \\ &+ \frac{\gamma_{\Delta\ell=1}}{s}\left(\frac{Y_{N_i}}{Y_{N_i}^{\text{eq}}} - 1\right)\Bigg],\end{aligned} \tag{19}$$

where $z = M_1/T$, and H is the Hubble parameter. As mentioned above, here we are considering two quasidegenerate RHNs to obtain a significant resonant enhancement in the CP asymmetry parameter. The remaining RHN (N_3) is chosen to have a large mass gap from these two quasidegenerate RHNs (N_1 and N_2) such that the effect of N_3 on the lepton asymmetry can be neglected. In the above, Y_i and $Y_{N_i}^{\text{eq}}$ ($i = 1, 2$) are the comoving number density and equilibrium comoving number density of N_i, respectively. The total decay width of N_i is $\Gamma_i = \sum_\alpha (\Gamma_{N_i\to\ell_\alpha H} + \Gamma_{N_i\to\overline{\ell}_\alpha \overline{H}})$, and the thermal averaged decay width $\langle\Gamma_i\rangle = \Gamma_i \text{K}_1(z)/\text{K}_2(z)$. The explicit form of Γ_i is given by

$$\Gamma_i = \frac{(Y_{\text{D}}^\dagger Y_{\text{D}})_{ii}}{16\pi} M_i, \tag{20}$$

where i is not summed over. The second term represents the change in the comoving number density of N_i due to Z_{BL} decaying into a pair of N_i, and the corresponding decay width is denoted by Γ_{BL}^{ii} with $Y_{Z_{\text{BL}}}^{\text{eq}}$ being the equilibrium comoving number density of the B − L gauge boson.

Apart from the decay, the abundance of N_i depends on the third-generation quarks[1] involving the $\Delta L_\alpha = 1$ scattering processes, and the effect of these processes in the evolution of N_i will appear through the quantity $\gamma_{\Delta L_\alpha=1}$, and it is defined as

$$\gamma_{\Delta\ell=1} = \gamma_{\ell_{\alpha_L} N_i}^{\bar{t}_R U_{3_L}} + \gamma_{U_{3_L} N_i}^{\ell_{\alpha_L} t_R} + \gamma_{t_R N_i}^{\overline{\ell}_{\alpha_L} U_{3_L}}. \tag{21}$$

The general form of γ_{kl}^{ij} for the scattering $ij \to kl$ is given by

$$\gamma_{kl}^{ij} = M_1^5 \frac{2\pi^2 T}{(2\pi)^6}\int_4^\infty dx \sqrt{x}\text{K}_1(\sqrt{x}z)\bar{\sigma}_{ij\to kl}, \tag{22}$$

where $\bar{\sigma}_{ij\to kl} \equiv 2 g_i g_j x \Lambda(1, \frac{r_i}{x}, \frac{r_j}{x})\sigma_{ij\to kl}$ with $\Lambda(a, b, c) = (a - b - c)^2 - 4bc$, and $r_i = \frac{M_i^2}{M_1^2}$. $g_i(g_j)$ and $M_i(M_j)$ are

[1]Here we have ignored the effect of the first- and second-generation quarks due to tiny Yukawa couplings.

the internal degrees of freedom and the mass of the initial state particle $i(j)$, respectively, and $\sigma_{ij\to kl}$ is the cross section of the $ij \to kl$ process.

Additionally, the abundance of N_i strongly depends on $g_{\rm BL}$ and Y_i through $Z_{\rm BL}$ and η_1 involving the scattering process, and the information of these processes is encoded in the quantity $\gamma_{\rm tot}$, which is given by

$$\gamma_{\rm tot} = \gamma^{N_iN_i}_{Z_{\rm BL}Z_{\rm BL}} + \gamma^{N_iN_i}_{\eta\eta} + \gamma^{N_iN_i}_{Z_{\rm BL}\eta}. \tag{23}$$

The explicit forms of $\bar{\sigma}_{ij\to kl}$ for the different processes mentioned in Eqs. (21) and (23) are given in Appendix B. We would like to note here that in deriving the Boltzmann equation of N_i, we have assumed that the BSM degrees of freedom, except the RHNs such as $Z_{\rm BL}$ and η, are in thermal equilibrium with the SM plasma. This can be achieved easily if we have either a sufficiently large gauge coupling $g_{\rm BL}$ or a large scalar mixing angle θ with the Higgs boson or both. The collision term of the Boltzmann equation for Y_{Δ_α} is composed of contributions coming from the decay and inverse decay of N_i's and other lepton-number-violating scatterings. The Boltzmann equation for the lepton flavor α can be written as

$$\frac{dY_{\Delta_\alpha}}{dz} = -\frac{1}{zH}\sum_i \Bigg[\langle\epsilon_{i\alpha}\Gamma_i\rangle(Y_{N_i} - Y^{\rm eq}_{N_i}) - \frac{\Delta Y_{\ell_{L_\alpha}}}{2Y^{\rm eq}_{\ell_\alpha}}\langle\Gamma^\alpha_i\rangle Y^{\rm eq}_{N_i} - \frac{1}{s}\frac{\Delta Y_{\ell_{L_\alpha}}}{Y^{\rm eq}_{\ell_\alpha}}\left(\frac{Y_{N_i}}{Y^{\rm eq}_{N_i}}\gamma^{\bar{l}_R U_{3L}}_{i\alpha} + \gamma^{\alpha t_R}_{iU_{3L}} + \gamma^{\bar{\alpha}U_{3L}}_{it_R}\right) + \mathcal{C}_{\rm LFV}\Bigg], \tag{24}$$

where on the right-hand side, we replace $\Delta Y_{\ell_{L_\alpha}}$ with Eq. (14).

Here, the first term is the creation of asymmetry in α flavor due to the decay of N_i into ℓ_{L_α} and the corresponding scalar, while the second term represents a washout of the created lepton asymmetry as a result of the inverse decay. The terms within the parenthesss are the contributions coming from the $\Delta L_\alpha = 1$ scattering processes in the evolution of the lepton asymmetry. The last $\mathcal{C}_{\rm LFV}$ term contains subdominant lepton-number-violating processes, and the explicit form of the collision terms are given in Appendix C.

The asymmetry generated from the decay of N_i into a particular flavor α is parametrized by a parameter called the CP asymmetry parameter, which is defined as

$$\epsilon_{i\alpha} = \frac{\Gamma_{N_i\to\ell_\alpha H} - \Gamma_{N_i\to\bar{\ell}_\alpha\bar{H}}}{\Gamma_i}, \tag{25}$$

where the summation over $SU(2)_L$ indices is implicit. The explicit form of $\epsilon_{i\alpha}$ in terms of the model parameters is as follows:

$$\epsilon_{i\alpha} = \frac{1}{8\pi(Y_{\rm D}^\dagger Y_{\rm D})_{ii}}\sum_{j\neq i}\Bigg[\sqrt{x_{ji}}\left(1 + (1+x_{ji})\log\frac{x_{ji}}{1+x_{ji}}\right)\kappa_1 + \frac{(1-x_{ji})}{(1-x_{ji})^2 + x_{ji}\mathcal{Y}_{ji}}\kappa_2\Bigg], \tag{26}$$

where

$$\kappa_1 = {\rm Im}[Y^*_{{\rm D}\alpha i}Y_{{\rm D}\alpha j}(Y_{\rm D}{}^T Y_{\rm D}{}^*)_{ji}],$$
$$\kappa_2 = {\rm Im}[Y^*_{{\rm D}\alpha i}Y_{{\rm D}\alpha j}(Y_{\rm D}{}^\dagger Y_{\rm D})_{ji}, + Y^*_{{\rm D}\alpha i}Y_{{\rm D}\alpha j}(Y_{\rm D}{}^T Y_{\rm D}{}^*)_{ji}\sqrt{x_{ji}}].$$

Here, $\mathcal{Y}_{ji} = \Gamma_j^2/M_i^2$, $x_{ji} = M_j^2/M_i^2$, and the index i is not summed over. At tree level, there is no CP asymmetry between the two decay modes ($N_i \to \ell_{L_\alpha}H$ and $N_i \to \bar{\ell}_{L_\alpha}\bar{H}$). However, an asymmetry can be generated due to the interference between the tree-level and one-loop-level diagrams when there are complex Yukawa couplings and more than one RHN. In the above expression of the CP asymmetry parameter, the first term represents interference between tree-level and vertex correction diagrams, while in the second term, a self-energy correction diagram is involved. The resonant enhancement occurs when the mass splitting between the two sterile states $M_i - M_j \simeq \frac{\Gamma_j}{2}$. In this case, the prefactor in the self-energy correction term becomes proportional to Γ_j^{-1}. In Fig. 1, the CP asymmetry parameter is demonstrated with the mass splitting $\Delta M \equiv M_2 - M_1$ for $M_1 = 3$ TeV. The solid lines represent the asymmetry generated from the decay of N_1 into two different lepton flavors like e, and μ. The dashed lines indicate similar quantities for the decay of the other RHN N_2. We would like to point out that there is a critical value of $\Delta M_{ij} \equiv M_i - M_j$ below which the asymmetry parameter behaves oppositely with the mass splitting. This happens when $(1-x_{ji})^2 \ll x_{ji}\mathcal{Y}_{ji}$ (i.e., $M_i - M_j < \frac{\Gamma_j}{2}$),

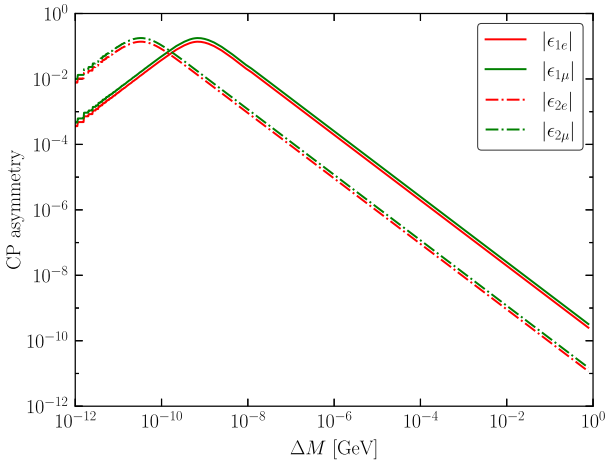


FIG. 1. Variation of CP asymmetry with mass splitting ΔM for $M_1 = 3$ TeV.

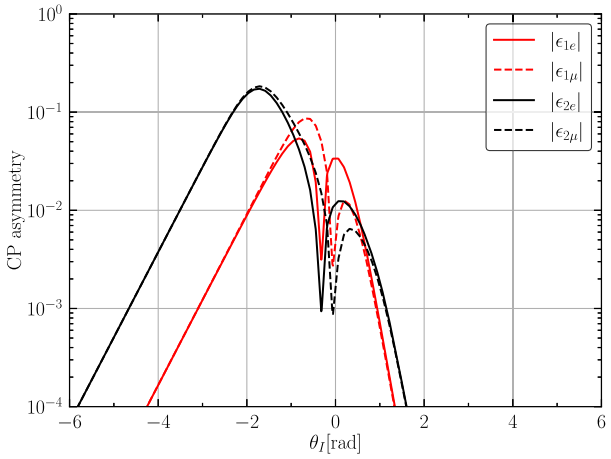


FIG. 2. Variation of CP asymmetry with θ_I for $M_1 = 3$ TeV, $\theta_R = 1$ rad, and $\Delta M = 1.3 \times 10^{-10}$ GeV.

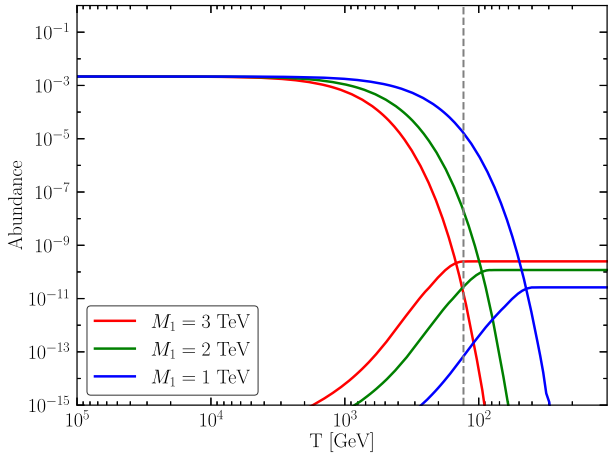


FIG. 3. Evolution of $Y_\Delta \equiv Y_{\Delta_e} + Y_{\Delta_\mu}$ as a function of T for $M_1 = 1$ TeV (blue), 2 TeV (green) and 3 TeV (red), respectively. The vertical dashed line denotes the sphaleron decoupling temperature.

TABLE I. Benchmark points for the FOPT which satisfy all the collider constraints. All the dimensionful quantities are in units of TeV.

	$m_{Z_{BL}}$	g_{BL}	m_η	$\sin\theta$	M_1	α	β/H_*	T_n
BP_1	11.40	1.01×10^{-1}	0.5	0.1	3.0	1.16×10^{-1}	13.60×10^3	1.36
BP_2	13.00	8.11×10^{-2}	0.5	0.1	3.0	1.01×10^{-1}	19.81×10^3	1.98
BP_3	13.36	7.62×10^{-2}	0.5	0.1	3.0	8.97×10^{-2}	21.85×10^3	2.18
BP_4	11.10	7.11×10^{-2}	0.5	0.1	3.0	3.97×10^{-2}	28.51×10^3	2.85
BP_5	11.90	6.31×10^{-2}	0.5	0.1	3.0	3.51×10^{-2}	35.08×10^3	3.51
BP_6	11.54	5.96×10^{-2}	0.5	0.1	3.0	2.82×10^{-2}	42.15×10^3	4.21

and in this case, the prefactor becomes proportional to ΔM_{ij}, i.e., $(1 - x_{ji})/x_{ji}\mathcal{Y}_{ji} \sim \Delta M_{ij} M_i/\Gamma_j^2$. This nature is seen in Fig. 1 where the critical value of the mass splitting is $\sim 10^{-10}$ GeV for $M_1 = 3$ TeV.

The asymmetry parameter also depends on θ_R and θ_I since Y_D depends on the R matrix given in Eq. (7). In order to understand the nontrivial dependence of $\epsilon_{i\alpha}$ on θ_R and θ_I, in Fig. 2, we have shown the variation of the asymmetry parameter as a function of θ_I for $\theta_R = 1$ rad. In this figure, the other parameters are fixed according the benchmark point 1 (BP1), as mentioned in Table I. As one can see from the figure, the CP asymmetry is peaked when $\theta_I < 0$. Thus, in the rest of our analysis, we have fixed $\theta_R = 1$ rad and $\theta_I = -1$ rad. Let us note in passing that we have also checked the dependence of $\epsilon_{i\alpha}$ on θ_R, and find that the dependence is mild.

Now, to calculate the baryon asymmetry, we have solved the Boltzmann equations for two RHNs and three lepton flavors [Eqs. (19) and (24)] numerically using Eqs. (20)–(23) and (26) to obtain the respective comoving abundance. In Fig. 3, we have demonstrated[2] $Y_\Delta \equiv Y_{\Delta_e} + Y_{\Delta_\mu}$ for three different values of $M_1 = 1$ TeV (blue), 2 TeV (green), and 3 TeV (red), respectively. From this plot, it is clearly seen that Y_Δ saturates before the sphaleron decoupling temperature ($\simeq$130 GeV) only when $M_1 \gtrsim 3$ TeV. For $M_1 \lesssim 3$ TeV, the lepton asymmetry saturates after the freeze-out of the sphaleron, and therefore, the former will not be converted into the baryon asymmetry efficiently. In the same plot, for completeness, we have also illustrated the abundance of N_1 for the three chosen values of M_1. Therefore, in the rest of our analysis, we fix $M_1 = 3$ TeV and $M_3 = 10$ TeV.

In Fig. 4, we have shown our results for six benchmark points listed in Table I. The black line represents the comoving abundance for the lightest RHN N_1. Since we are considering a resonant enhancement in the CP asymmetry parameter, N_2 is almost degenerate to N_1, and hence its evolution is identical to the lightest RHN; therefore, we have not shown Y_{N_2} separately. The comoving abundances for Y_{Δ_α} ($\alpha = e$ and μ) are indicated by green and blue lines, respectively. As we have seen for the asymmetry parameter (Fig. 1), a similar nature is reflected in the comoving abundance also, i.e., $Y_{\Delta_e} \gtrsim Y_{\Delta_\mu}$.

To understand the relative magnitudes of the various decay, inverse decay, and $2 \to 2$ scatterings in the collision terms, we have plotted γ as a function of z in Fig. 5. Finally, the baryon-to-photon ratio (η_B), an experimentally obtained physical quantity, can be determined from Y_{Δ_α} using Eq. (18). For all benchmark points, η_B is obtained within the 2σ range of experimental measurement by suitably adjusting the mass gap between the two quasidegenerate RHNs. As an example, for BP1, BP2, and BP3, the mass gap $\Delta M = 1.3 \times 10^{-10}$ GeV, 2.65×10^{-10} GeV, and 3.3×10^{-10} GeV, respectively,

[2] Y_{Δ_τ} vanishes as the CP asymmetry parameters for the third-generation leptons are identically zero.

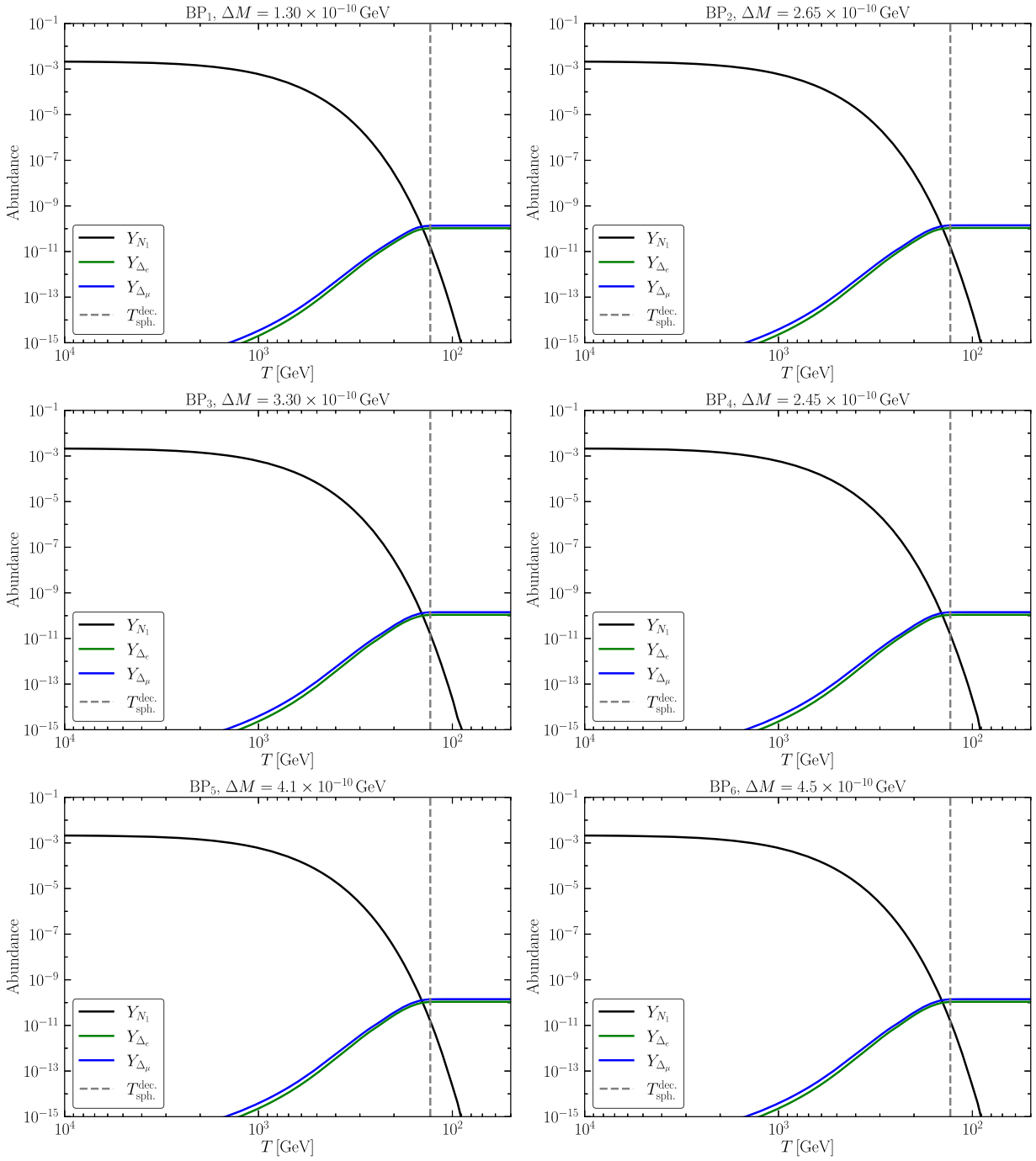


FIG. 4. Evolution of comoving number densities with T for the six benchmark points. The gray dashed vertical line in each panel denotes the sphaleron decoupling temperature $T_{\rm sph}^{\rm dec} = 130$ GeV.

while $\Delta M = 2.45 \times 10^{-10}$ GeV, 4.1×10^{-10} GeV, and 4.5×10^{-10} GeV, respectively, for the other three benchmark points.

In the next section, we will discuss the production of the SGWB from an FOPT and the prospects of probing the parameter space of resonant flavored leptogenesis in future GW detectors.

V. FIRST-ORDER PHASE TRANSITION AND GRAVITATIONAL WAVE

In the SM, the phase transition is a crossover type, and thus the presence of an extra scalar field in the scalar sector makes the dynamics more intriguing. In this section, we discuss the dynamics of the first-order transition when the scalar sector contains a complex scalar field with a nonzero

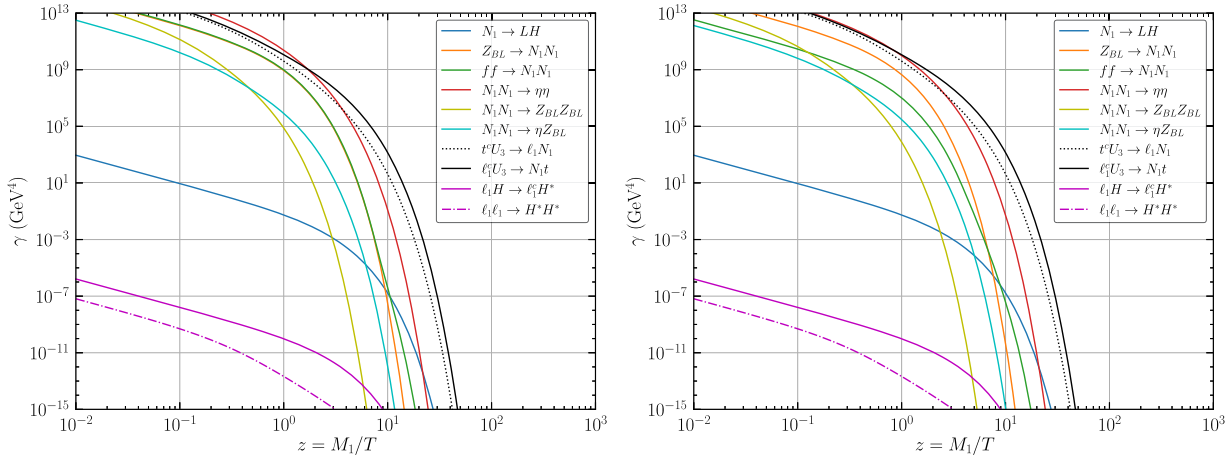


FIG. 5. γ as a function of z for the processes relevant in the Boltzmann equation for BP1 (left panel) and BP3 (right panel).

$U(1)_{\mathrm{B-L}}$ quantum number. The presence of an extra scalar field and a $U(1)_{\mathrm{B-L}}$ gauge boson can generate GW signals, which can be detected in upcoming GW detectors. In the following sections, we discuss our scalar potential, dynamics of first-order phase transition, and GW signals. First, we start our discussion with a description of the scalar potential.

A. Scalar potential in the thermal background

The tree-level potential in terms of ζ_1 and η_1 is as follows:

$$V_{\mathrm{Tree}} = -\frac{\mu_H^2}{2}\zeta_1^2 - \frac{\mu_\Phi^2}{2}\eta_1^2 + \frac{\lambda_H}{4}\zeta_1^4 + \frac{\lambda_\Phi}{4}\eta_1^4 - \frac{\lambda'}{4}\zeta_1^2\eta_1^2. \tag{27}$$

The one-loop corrected potential of Eq. (27) in the thermal background has two parts: (i) the one-loop corrected potential at zero temperature known as the Coleman-Weinberg (CW) potential (V_{CW}) [112] and (ii) the temperature-dependent part of the one-loop correction ($V_{T\neq 0}$). First, we will discuss the CW potential for our model. The CW potential of our model in the Landau gauge is given by

$$\begin{aligned} V_{\mathrm{CW}} = \frac{1}{64\pi^2}\Bigg[& \bar{m}_\zeta^4\left(\ln\left(\frac{\bar{m}_\zeta^2}{\mu^2}\right) - \frac{3}{2} + C_{\mathrm{UV}}\right) + \bar{m}_\eta^4\left(\ln\left(\frac{\bar{m}_\eta^2}{\mu^2}\right) - \frac{3}{2} + C_{\mathrm{UV}}\right) + 2\bar{m}_{G^+}^4\left(\ln\left(\frac{\bar{m}_{G^+}^2}{\mu^2}\right) - \frac{3}{2} + C_{\mathrm{UV}}\right) \\ & + \bar{m}_{\zeta_2}^4\left(\ln\left(\frac{\bar{m}_{\zeta_2}^2}{\mu^2}\right) - \frac{3}{2} + C_{\mathrm{UV}}\right) + \bar{m}_{\eta_2}^4\left(\ln\left(\frac{\bar{m}_{\eta_2}^2}{\mu^2}\right) - \frac{3}{2} + C_{\mathrm{UV}}\right) + 6\bar{m}_W^4\left(\ln\left(\frac{\bar{m}_W^2}{\mu^2}\right) - \frac{5}{6} + C_{\mathrm{UV}}\right) \\ & + 3\bar{m}_Z^4\left(\ln\left(\frac{\bar{m}_Z^2}{\mu^2}\right) - \frac{5}{6} + C_{\mathrm{UV}}\right) + 3\bar{m}_{Z_{\mathrm{BL}}}^4\left(\ln\left(\frac{\bar{m}_{Z_{\mathrm{BL}}}^2}{\mu^2}\right) - \frac{5}{6} + C_{\mathrm{UV}}\right) - 12\bar{m}_t^4\left(\ln\left(\frac{\bar{m}_t^2}{\mu^2}\right) - \frac{3}{2} + C_{\mathrm{UV}}\right) \\ & - 2\sum_{i=1}^{3}\bar{m}_i^4\left(\ln\left(\frac{\bar{m}_i^2}{\mu^2}\right) - \frac{3}{2} + C_{\mathrm{UV}}\right)\Bigg], \end{aligned} \tag{28}$$

where μ is the renormalization scale and we consider $\mu = v_{\mathrm{BL}}$. The field-dependent masses of the SM and BSM degrees of freedoms are denoted by $\bar{m}$, and they are listed in Appendix D. We would like to mention that the form of Eq. (28) is gauge dependent, and a gauge-independent study is beyond the scope of this work (see [113,114] for a gauge-independent analysis). We confined our analysis in the Landau gauge ($\xi = 0$) so that the contributions of the ghosts were absent in V_{CW} [115]. $C_{\mathrm{UV}} = -(2/\epsilon - \gamma + \log 4\pi)$ in the CW potential contains the divergent part, which will be removed by introducing the following counterterm Lagrangian:

$$V_{\mathrm{CT}} = -\frac{\delta_{\mu_H}}{2}\zeta_1^2 - \frac{\delta_{\mu_\Phi}}{2}\eta_1^2 + \frac{\delta_{\lambda_H}}{4}\zeta_1^4 + \frac{\delta_{\lambda_\Phi}}{4}\eta_1^4 - \frac{\delta_{\lambda'}}{4}\zeta_1^2\eta_1^2. \tag{29}$$

We impose the following renormalization conditions to determine the unknown coefficients of Eq. (29):

$$\frac{\partial(V_{\rm CW}+V_{\rm CT})}{\partial\zeta_1}=0, \qquad \frac{\partial(V_{\rm CW}+V_{\rm CT})}{\partial\eta_1}=0,$$
$$\frac{\partial^2(V_{\rm CW}+V_{\rm CT})}{\partial\zeta_1^2}=0, \qquad \frac{\partial^2(V_{\rm CW}+V_{\rm CT})}{\partial\eta_1^2}=0,$$
$$\frac{\partial^2(V_{\rm CW}+V_{\rm CT})}{\partial\zeta_1\partial\eta_1}=0, \tag{30}$$

where the first two conditions ensure that the loop correction does not alter the tree-level vacua, and the last three conditions make the tree-level scalar mass matrix unaltered. Solving Eq. (30), we obtain

$$\delta_{\mu_H}=\frac{3V_{\rm CW}^{\zeta_1}-v_{\rm BL}V_{\rm CW}^{\zeta_1\eta_1}-v_hV_{\rm CW}^{\zeta_1\zeta_1}}{2v_h},$$
$$\delta_{\mu_\Phi}=\frac{3V_{\rm CW}^{\eta_1}-v_hV_{\rm CW}^{\zeta_1\eta_1}-v_{\rm BL}V_{\rm CW}^{\eta_1\eta_1}}{2v_{\rm BL}},$$
$$\delta_{\lambda_H}=\frac{V_{\rm CW}^{\zeta_1}-v_hV_{\rm CW}^{\zeta_1\zeta_1}}{2v_h^3},$$
$$\delta_{\lambda_\Phi}=\frac{V_{\rm CW}^{\eta_1}-v_{\rm BL}V_{\rm CW}^{\eta_1\eta_1}}{2v_{\rm BL}^3}, \qquad \delta_{\lambda'}=\frac{V_{\rm CW}^{\zeta_1\eta_1}}{v_hv_{\rm BL}}, \tag{31}$$

where $V_{\rm CW}^{x,y}\equiv\frac{\partial^2V_{\rm CW}}{\partial x\partial y}$ is calculated at the vacuum configuration. Note that the Goldstone bosons are massless at the physical vacuum, and it makes the calculation unstable once we calculate the derivatives of $V_{\rm CW}$ at the vacuum configuration. In our calculation, this problem is circumvented by adding a regulator mass $m_{\rm IR}$ to the field-dependent Goldstone boson mass $\bar{m}_G$ as $\bar{m}_G^2\to\bar{m}_G^2+m_{\rm IR}^2$. Here, we took $m_{\rm IR}^2=10\ {\rm GeV}^2$, which is much smaller than the mass scale of the other degrees of freedom. However, in our numerical analysis, the derivatives of $V_{\rm CW}$ are calculated using the finite-difference method [116], and the choice of the increment of the independent variable serves as a regulator and it prevents the function $V_{\rm CW}$ from encountering the singularity at the physical vacuum.

In the thermal background, the scalar potential can be derived from the following Eq. [117]:

$$V_{\rm 1-loop}^{\rm total}=\sum_B\frac{g_BT}{2}\sum\!\!\!\!\!\!\int_{n_b=0}^{\infty}\frac{d^3\vec{k}}{(2\pi)^3}\ln(\omega_{n_b}^2+\omega^2)$$
$$-\sum_F\frac{g_FT}{2}\sum\!\!\!\!\!\!\int_{n_f=0}^{\infty}\frac{d^3\vec{k}}{(2\pi)^3}\ln(\omega_{n_f}^2+\omega^2), \tag{32}$$

where the summation over B and F runs over all bosons and fermions. T is the plasma temperature and $\omega^2=|\vec{k}|^2+\bar{m}^2$. $\omega_b=2\pi n_bT$ and $\omega_f=(2n_f+1)\pi T$ are Matsubara frequencies for the boson and fermions, respectively. The coefficients $g_B=1,\ 2,\ 3,\ 4,\ 2$ for the real scalar, complex scalar, massive gauge boson, Dirac fermion, and Majorana fermion, respectively. After performing the Matsubara frequency sum, one can write Eq. (32) as

$$V_{\rm 1-loop}^{\rm total}(\zeta_1,\eta_1)=V_{\rm CW}(\zeta_1,\eta_1)+V_{T\neq0}(\zeta_1,\eta_1), \tag{33}$$

where

$$V_{T\neq0}(\zeta_1,\eta_1)=\frac{T^4}{2\pi^2}\left[\sum_Bg_BJ_B\left(\frac{\bar{m}_B^2}{T^2}\right)-\sum_Fg_BJ_F\left(\frac{\bar{m}_F^2}{T^2}\right)\right]. \tag{34}$$

The explicit form of $J_B(x_B)$ and $J_F(x_F)$ is as follows:

$$J_B(x)=\int_0^\infty dz\,z^2\ln\left(1-\exp\left(-\sqrt{z^2+x}\right)\right),$$
$$J_F(x)=\int_0^\infty dz\,z^2\ln\left(1+\exp\left(-\sqrt{z^2+x}\right)\right). \tag{35}$$

Lastly, the bosonic sum in Eq. (32) becomes infrared (IR) divergent due to the presence of the $n_b=0$ contribution in the first term, and the perturbative expansion becomes unreliable. In order to circumvent this IR divergence, we need to resum the thermal mass of the bosonic degrees of freedom. We follow the Arnold-Espinosa method [118] and add the following to the scalar potential[3]:

$$V_{\rm daisy}=\sum_B\frac{g_BT}{12\pi}[\bar{m}_B^3-\bar{m}_{B,T}^3], \tag{36}$$

where the summation runs over all the bosonic degrees of freedom, and $\bar{m}_{B,T}$ is the field-dependent mass of the bosonic fields in the thermal background. The explicit forms of $\bar{m}_{B,T}$ for all the bosonic degrees of freedom are given in Appendix D. Let us note that, for gauge bosons, the value of g_B in Eq. (36) is 1 since only longitudinal modes acquire thermal mass.

Thus, the total scalar potential in our case is given by

$$V_{\rm total}=V_{\rm tree}+V_{\rm CW}+V_{\rm CT}+V_{T\neq0}+V_{\rm daisy}. \tag{37}$$

In the next section, we will discuss some important features of Eq. (37) and the production of the GW signal.

B. FOPT dynamics and GW signal

Before delving into our numerical results, we use our tree-level and thermal potential in order to understand the FOPT dynamics in the presence of an extra scalar with a nonzero $U(1)_{\rm B-L}$ charge. Neglecting $V_{\rm CW}$ and $V_{\rm daisy}$, in the high-temperature limit, we can write Eq. (37) as

[3]Resummation of the thermal mass of fermionic fields is not required since the fermionic summation in Eq. (32) is not IR divergent because $\omega_{n_f}\neq0$ for $n_f=0$.

$$V_{\text{total}} \simeq \frac{1}{2}(-\mu_H^2 + c_H T^2)\zeta_1^2 + \frac{1}{2}(-\mu_\Phi^2 + c_\Phi T^2)\eta_1^2 - E_H \zeta_1^3 T - E_\Phi \eta_1^3 T + \frac{\lambda_H}{4}\zeta_1^4 + \frac{\lambda_\Phi}{4}\eta_1^4 - \frac{\lambda'}{4}\zeta_1^2\eta_1^2, \quad (38)$$

where

$$c_H = \left(\frac{g_1^2}{16} + \frac{3g_2^2}{16} + \frac{y_t^2}{4} + \frac{\lambda_H}{2} - \frac{\lambda'}{12}\right),$$
$$c_\Phi = \left(g_{\text{BL}}^2 + \frac{y_N^2}{8} + \frac{\lambda_\Phi}{3} - \frac{\lambda'}{6}\right),$$
$$E_H = \frac{m_W^3}{2\pi v_h^3} + \frac{m_Z^3}{4\pi v_h^3}, \qquad E_\Phi = \frac{m_{Z_{\text{BL}}}^3}{4\pi v_{\text{BL}}^3}. \quad (39)$$

At high temperature, both EW and $U(1)_{\text{B-L}}$ symmetries are restored due to the temperature-dependent coefficients of ζ_1^2 and η_1^2. However, as the Universe cools down, a phase transition occurs. First, we start our discussion with $g_{\text{BL}} \to 0$, which implies that E_Φ vanishes. The absence of E_Φ implies that the FOPT occurs in the ζ_1 direction only. In this limit, a first-order electroweak phase transition (FOEWPT) occurs when

$$\frac{v_c}{T_c} = \frac{8E_H\lambda_\phi}{4\lambda_H\lambda_\Phi - \lambda'^2}, \quad (40)$$

where v_c is the EW VEV at critical temperature T_c. If we substitute all the quartic couplings given in Eq. (40), we will find that the ratio v_c/T_c is greater than 1 when the mixing angle is large and $m_\eta < m_\zeta$. However, in our parameter space of interest, the mass of the extra scalar is larger than the SM Higgs, and as a result, FOEWPT is not possible in our scenario. In spite of this, we can still have an FOPT in the η_1 direction, thanks to $g_{\text{BL}} \neq 0$, and as a result, SGWB can be generated. In the next section, we will discuss the SGWB signal originated from the FOPT and present our numerical results.

C. Stochastic gravitational wave background from the FOPT

The amplitude of the SGWB emitted from the FOPT has three sources, and the total amplitude is

$$\Omega_{\text{GW}}h^2 = \Omega_{\text{coll}}h^2 + \Omega_{\text{sw}}h^2 + \Omega_{\text{MHD}}h^2, \quad (41)$$

where individual contributions from the bubble-wall collision ($\Omega_{\text{coll}}h^2$), sound waves in the plasma using an envelope approximation ($\Omega_{\text{sw}}h^2$), and magnetohydrodynamic turbulence in the plasma ($\Omega_{\text{turb}}h^2$) are as follows [119].

The contribution to the GW amplitude from the bubble-wall collision is

$$\Omega_{\text{GW}}h^2 = 1.67 \times 10^{-5}\left(\frac{H_*}{\beta}\right)^2\left(\frac{\kappa\alpha}{1+\alpha}\right)^2\left(\frac{100}{g_*(T_n)}\right)^{1/3} \times \left(\frac{0.11 v_w^3}{0.42 + v_w^2}\right)\left(\frac{3.8(f/f_{\text{col}})^{2.8}}{1 + 2.8(f/f_{\text{col}})^{3.8}}\right), \quad (42)$$

with the peak frequency of the spectrum

$$f_{\text{col}} = 1.65 \times 10^{-5}\ \text{Hz}\left(\frac{0.62}{1.8 - 0.1 v_w + v_w^2}\right)\left(\frac{\beta}{H_*}\right) \times \left(\frac{T_n}{100\ \text{GeV}}\right)\left(\frac{g_*(T_n)}{100}\right)^{1/6}. \quad (43)$$

The contribution of the sound wave after the bubble collision is

$$\Omega_{\text{sw}}h^2 = 2.65 \times 10^{-6}\left(\frac{H_*}{\beta}\right)\left(\frac{\kappa_v\alpha}{1+\alpha}\right)^2\left(\frac{100}{g_*(T_n)}\right)^{1/3} \times v_w\left(\frac{f}{f_{\text{sw}}}\right)^3\left(\frac{7}{4 + 3(f/f_{\text{sw}})^2}\right)^{7/2}, \quad (44)$$

and in this case, the peak frequency is

$$f_{\text{sw}} = 1.9 \times 10^{-5}\ \text{Hz}\, v_w^{-1}\left(\frac{\beta}{H_*}\right)\left(\frac{T_n}{100\ \text{GeV}}\right)\left(\frac{g_*(T_n)}{100}\right)^{1/6}. \quad (45)$$

Lastly, the contribution from $\Omega_{\text{MHD}}h^2$ is given by

$$\Omega_{\text{MHD}}h^2 = 3.35 \times 10^{-4}\left(\frac{H_*}{\beta}\right)\left(\frac{\kappa_{\text{turb}}\alpha}{1+\alpha}\right)^{3/2}\left(\frac{100}{g_*(T_n)}\right)^{1/3} \times \left(\frac{v_w(f/f_{\text{turb}})^3}{[1 + (f/f_{\text{turb}})]^{11/3}(1 + 8\pi f/h_*)}\right), \quad (46)$$

where

$$h_* = 1.65 \times 10^{-5}\ \text{Hz}\left(\frac{T_n}{100\ \text{GeV}}\right)\left(\frac{g_*(T_n)}{100}\right)^{1/6}, \quad (47)$$

and the peak frequency

$$f_{\text{turb}} = 2.7 \times 10^{-5}\ \text{Hz}\, v_w^{-1}\left(\frac{\beta}{H_*}\right)\left(\frac{T_n}{100\ \text{GeV}}\right)\left(\frac{g_*(T_n)}{100}\right)^{1/6}. \quad (48)$$

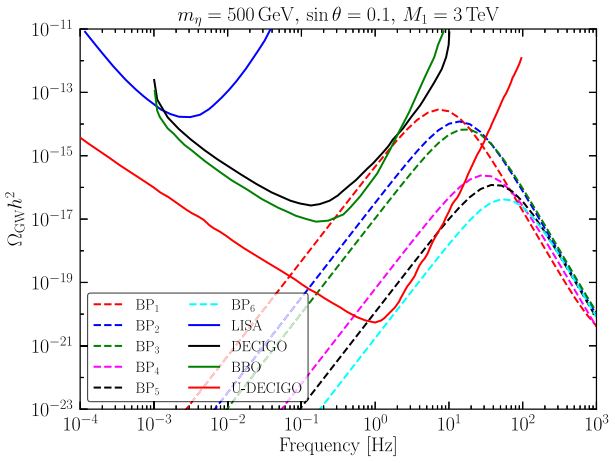


FIG. 6. Frequency spectrum of SGWB for six benchmark points tabulated in Table I. Here, we fix $m_\eta = 500$ GeV, $\sin\theta = 0.1$. The sensitivity curves of LISA, DECIGO, BBO, and U-DECIGO are shown by blue, black, green, and red lines, respectively. The data for the sensitivity curves are taken from [44,126].

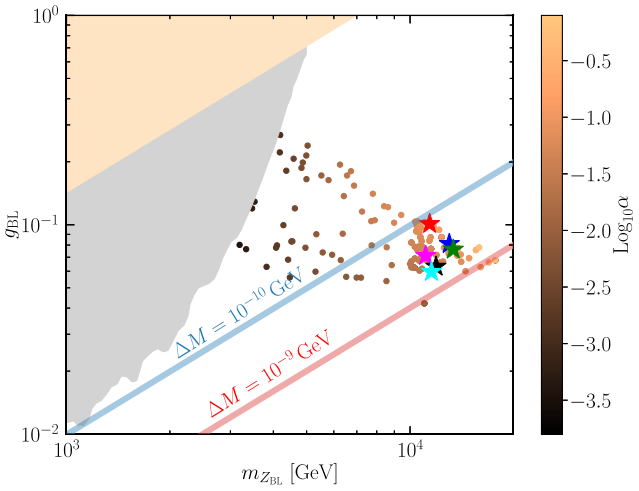


FIG. 7. Parameter space in the $m_{Z_{BL}} - g_{BL}$ plane for $m_\eta = 500$ GeV, $\sin\theta = 0.1$, $M_1 = 3$ TeV. The scattered points represent the FOPT, and the strength of the transition (α) is depicted by the color bar. The gray region is excluded from the dilepton search at the LHC, and the yellow region is disallowed from the measurement of the $e^+e^- \to \ell^+\ell^-$ search at the LEP. Observed baryon asymmetry at 2σ confidence interval can be explained within the blue and red bands for $\Delta M = 10^{-10}$ GeV and $\Delta M = 10^{-9}$ GeV, respectively. The benchmark points given in Table I are denoted by $\star$, and their color code is the same as Fig. 6.

The bubble-wall speed is given by[4]

$$v_w = \frac{\sqrt{1/3} + \sqrt{\alpha^2 + 2\alpha/3}}{1+\alpha}, \tag{49}$$

and we use

$$\kappa = \frac{0.715\alpha + (4/27) * \sqrt{3\alpha/2}}{1 + 0.715\alpha},$$
$$\kappa_v = \frac{\alpha}{0.73 + 0.083\sqrt{\alpha} + \alpha},$$
$$\kappa_{\rm turb} = 0.1\kappa_v. \tag{50}$$

In Eqs. (42)–(46), T_n is the bubble nucleation temperature, β^{-1} is the duration of the FOPT, and α is the latent heat released during the transition, and they are defined as [123]

$$\alpha = \left(\frac{\Delta V_{\rm total} - T\frac{\partial \Delta V_{\rm total}}{\partial T}}{\rho_{\rm rad}}\right)_{T=T_n},$$
$$\beta = H_*\left(T\frac{d}{dT}\left(\frac{S_E}{T}\right)\right)_{T=T_n}, \tag{51}$$

where $V_{\rm total}$ is given in Eq. (37), $\Delta V_{\rm total}$ is the potential difference between the false and true vacuum, H_* is the Hubble parameter at T_n, and S_E is the three-dimensional Eucledian action [124]. These three quantities depend on the model parameters, and to identify the parameter space for the FOPT, we implemented our model in the publicly available CosmoTransitions code [125]. We scan $m_{Z_{BL}}$ between 1 and 20 TeV and g_{BL} between 10^{-2} and 1.0. The other parameters like the BSM scalar mass and scalar mixing angle are kept fixed at $m_\eta = 500$ GeV, $M_1 = 3$ TeV, and $\sin\theta = 0.1$, respectively.

In Fig. 6, we show the frequency spectrum of the emitted SGWB for six benchmark points, which are tabulated in Table I. These points are allowed from the collider constraints at 95% CL, and they can also explain the observed baryon asymmetry. The sensitivity curves of LISA, DECIGO, BBO, and U-DECIGO are shown by the blue, black, green, and red solid lines, respectively. As one can see from the figure that the amplitude of the emitted SGWB increases with α. This is because a larger value of α implies that the amount of emitted latent heat is large, and thus the strength of the SGWB is large as well. However, the peak frequency anticorrelates with α, and this can be understood as follows: For larger α, the energy difference between false and true vacuum is large, which implies that nucleation happens at a lower temperature. Since the peak frequency is directly proportional to T_n, it decreases with the increase in α.

In Fig. 7, we show the allowed region of parameter space in the $m_{Z_{BL}} - g_{BL}$ plane where we fix

[4]For $\alpha \gtrsim 0.1$, the wall speed becomes ultrarelativistic [120–122]. However, it does not change the GW prediction significantly, even if we use the Chapman-Jouguet velocity given in Eq. (49).

$m_\eta = 500$ GeV, $\sin\theta = 0.1$, and $M_1 = 3$ TeV and $M_3 = 10$ TeV, as discussed earlier. The constraint from the dilepton search at the LHC is shown by the gray region, and the corresponding LEP bound is shown by the light orange region as discussed in Sec. III. Here, one can see that for fixed $m_{Z_{\rm BL}}$, α is an increasing function of $g_{\rm BL}$. This is because for the FOPT in the η_1 direction, the order parameter is proportional to $g_{\rm BL}$ for the fixed value of $m_{Z_{\rm BL}}$. As a result, we get larger α for higher values of $g_{\rm BL}$. The blue and red bands denote the parameter space at which the observed baryon asymmetry can be explained within the 2σ confidence interval. One can clearly see that for[5] $M_1 \simeq M_2 = 3$ TeV and $M_3 = 10$ TeV, $Z_{\rm BL}$ with mass $\sim$10 TeV and $g_{\rm BL} \sim 0.1$ can produce an SGWB and successfully explain the observed baryon asymmetry of the Universe when the mass splitting ΔM varies between 10^{-10} and 10^{-9} GeV. Importantly, despite being inaccessible to the current collider experiments, this region of parameter space can be tested by the future GW detectors.

VI. SUMMARY AND CONCLUSIONS

In this work, we have considered a gauged $U(1)_{\rm B-L}$ extension of the SM which contains three RHNs (N_i), one gauge boson $Z_{\rm BL}$, and a complex scalar Φ in the particle spectrum. One RHN per lepton flavor is the minimal requirement for gauge anomaly cancellation, while a massive $Z_{\rm BL}$ and a CP-even scalar are natural consequences of spontaneously broken $U(1)_{\rm B-L}$ gauge symmetry. The presence of RHNs naturally accommodates sub-eV scale Majorana masses of SM neutrinos as well as explains the observed baryon asymmetry of the Universe. Here, we consider the TeV scale RHNs, and this can be achieved by choosing the breaking scale of $U(1)_{\rm B-L}$ and Y_i appropriately.

In this framework, CP asymmetry in the leptonic sector due to the decay of TeV scale RHNs with a hierarchical mass spectrum is not sufficient to produce correct baryon asymmetry. Thus, our scenario requires a significant boost in the CP asymmetry parameter, which is eventually possible by virtue of two quasidegenerate RHNs through resonant enhancement. Moreover, the dynamics of RHNs is heavily influenced by the new gauge boson $Z_{\rm BL}$ and the scalar Φ. We have calculated the abundance of RHNs taking into account all possible interaction channels involving $Z_{\rm BL}$, Φ, and a top quark. Furthermore, in TeV scale, since all the Yukawa interactions of the SM leptons are in equilibrium, one has to consider the effect of each lepton flavor in the asymmetry calculation separately, requiring the solution of five coupled Boltzmann equations simultaneously. We find the correct baryon asymmetry for a wide range of $m_{Z_{\rm BL}}$ which is beyond the reach of the present sensitivity of the LHC.

[5]This mass hierarchy requires $Y_{1,2} \simeq 0.08$, whereas $Y_3 \simeq 0.3$.

Future GW detectors have the potential to probe a part of the allowed region of the parameter space which is inaccessible to the current colliders. The presence of the $U(1)_{\rm B-L}$ breaking scalar opens up the possibility to test the model under consideration by producing an SGWB via an FOPT. The symmetry-breaking scale is related to the frequency of an emitted SGWB as well as the masses of an RHN and $Z_{\rm BL}$, which plays a crucial role in explaining the baryon asymmetry of our Universe. Leveraging the interconnection, we have investigated resonant leptogenesis in conjunction with the production of an SGWB from an FOPT. We identify the model parameter space that can explain the observed baryon asymmetry while producing an observable SGWB that can be detected in BBO, DECIGO, and U-DECIGO. We also discuss current constraints from the collider and the complementarity between the collider searches and GW detection.

ACKNOWLEDGMENTS

The work of S. G. was supported by the IBS under Project No. IBS-R018-D1. We would like to thank Abhijit Kumar Saha, Benoit Laurent, Carroll Wainwright, Francesco Costa, and Pankaj Borah for useful communication related to the CosmoTransitions package.

DATA AVAILABILITY

The data that support the findings of this article are not publicly available upon publication because it is not technically feasible and/or the cost of preparing, depositing, and hosting the data would be prohibitive within the terms of this research project. The data are available from the authors upon reasonable request.

APPENDIX A: FORMULATION OF THE $\mathcal{A}$ MATRIX

In this appendix, we will derive the structure of the $\mathcal{A}$ matrix used in Eq. (14).

The asymmetry between the number density of particle X and its antiparticle $\bar{X}$ can be written as

$$n_X - n_{\bar{X}} \simeq \frac{T^3}{6}\begin{cases} \frac{2g_X\mu_X}{T} & \text{for bosons,} \\ \frac{g_X\mu_X}{T} & \text{for fermions.} \end{cases} \tag{A1}$$

Here, $g_X = \{6, 3, 3, 2, 1, 2\}$ is the degree of the SM field content $\{Q_{L_i}, u_{R_i}, d_{R_i}, \ell_{L_i}, \ell_{R_i}, H\}$.

At the temperature when all the SM Yukawa couplings are in thermal equilibrium, it gives

$$\begin{aligned} &\mu_{\ell_{L_1}} - \mu_{\ell_{R_1}} - \mu_H = 0, \qquad \mu_{\ell_{L_2}} - \mu_{\ell_{R_2}} - \mu_H = 0, \\ &\mu_{\ell L_3} - \mu_{\ell_{R_3}} - \mu_H = 0, \end{aligned} \tag{A2}$$

$$\mu_{Q_{L_1}} - \mu_{d_{R_1}} - \mu_H = 0, \qquad \mu_{Q_{L_2}} - \mu_{d_{R_2}} - \mu_H = 0, \qquad \mu_{Q_{L_3}} - \mu_{d_{R_3}} - \mu_H = 0, \tag{A3}$$

$$\mu_{Q_{L_1}} - \mu_{u_{R_1}} + \mu_H = 0, \qquad \mu_{Q_{L_2}} - \mu_{u_{R_2}} + \mu_H = 0, \qquad \mu_{Q_{L_3}} - \mu_{u_{R_3}} + \mu_H = 0, \tag{A4}$$

where $\mu_{Q_{L_i}}$, $\mu_{u_{R_i}}$, $\mu_{d_{R_i}}$, $\mu_{\ell_{L_i}}$, $\mu_{\ell_{R_i}}$, μ_H are the chemical potentials of $Q_{L_i}, u_{R_i}, d_{R_i}, \ell_{L_i}, \ell_{R_i}, H$, respectively, and $i = 1\ldots3$.

The hypercharge neutrality condition gives

$$\begin{aligned} &4(\mu_{u_{R_1}} + \mu_{u_{R_2}} + \mu_{u_{R_3}}) + 2(\mu_{Q_{L_1}} + \mu_{Q_{L_2}} + \mu_{Q_{L_3}}) - 2(\mu_{\ell_{L_1}} + \mu_{\ell_{L_2}} + \mu_{\ell_{L_3}}) \\ &- 2(\mu_{d_{R_1}} + \mu_{d_{R_2}} + \mu_{d_{R_3}}) - 2(\mu_{\ell_{R_1}} + \mu_{\ell_{R_2}} + \mu_{\ell_{R_3}}) + 4\mu_H = 0. \end{aligned} \tag{A5}$$

An electroweak sphaleron populates an equal amount of left chiral quarks in each generation. Hence, the baryon number is equal in each generation, and it implies

$$2\mu_{Q_{L_1}} + \mu_{u_{R_1}} + \mu_{d_{R_1}} = 2\mu_{Q_{L_2}} + \mu_{u_{R_2}} + \mu_{d_{R_2}} = 2\mu_{Q_{L_3}} + \mu_{u_{R_3}} + \mu_{d_{R_3}}. \tag{A6}$$

The equilibrium of the electroweak and QCD sphaleron gives the following conditions:

$$\mu_{\ell_{L_1}} + \mu_{\ell_{L_2}} + \mu_{\ell_{L_3}} + 3(\mu_{Q_{L_1}} + \mu_{Q_{L_2}} + \mu_{Q_{L_3}}) = 0, \tag{A7}$$

$$2(\mu_{Q_{L_1}} + \mu_{Q_{L_2}} + \mu_{Q_{L_3}}) - (\mu_{u_{R_1}} + \mu_{u_{R_2}} + \mu_{u_{R_3}}) - (\mu_{d_{R_1}} + \mu_{d_{R_2}} + \mu_{d_{R_3}}) = 0. \tag{A8}$$

Note that Eq. (A8) is not an independent constraint since it can be derived by summing Eqs. (A3) and (A4).

Thus, we have 13 constraint equations, and they are given by Eqs. (A2)–(A7). Solving these equations, we can write $\mu_{Q_{L_i}}$, $\mu_{u_{R_i}}$, $\mu_{d_{R_i}}$, $\mu_{\ell_{R_i}}$, μ_H in terms of $\mu_{\ell_{L_i}}$ as

$$\begin{aligned} &\mu_{Q_{L_1}} = \mu_{Q_{L_2}} = \mu_{Q_{L_3}} = -\frac{1}{9}(\mu_{\ell_{L_1}} + \mu_{\ell_{L_2}} + \mu_{\ell_{L_3}}), \\ &\mu_{u_{R_1}} = \mu_{u_{R_2}} = \mu_{u_{R_3}} = \frac{5}{63}(\mu_{\ell_{L_1}} + \mu_{\ell_{L_2}} + \mu_{\ell_{L_3}}), \\ &\mu_{d_{R_1}} = \mu_{d_{R_2}} = \mu_{d_{R_3}} = -\frac{19}{63}(\mu_{\ell_{L_1}} + \mu_{\ell_{L_2}} + \mu_{\ell_{L_3}}), \\ &\mu_{\ell_{R_1}} = \frac{1}{21}(17\mu_{\ell_{L_1}} - 4\mu_{\ell_{L_2}} - 4\mu_{\ell_{L_3}}), \qquad \mu_{\ell_{R_2}} = \frac{1}{21}(-4\mu_{\ell_{L_1}} + 17\mu_{\ell_{L_2}} - 4\mu_{\ell_{L_3}}), \qquad \mu_{\ell_{R_3}} = \frac{1}{21}(-4\mu_{\ell_{L_1}} - 4\mu_{\ell_{L_2}} + 17\mu_{\ell_{L_3}}), \\ &\mu_H = \frac{4}{21}(\mu_{\ell_{L_1}} + \mu_{\ell_{L_2}} + \mu_{\ell_{L_3}}), \end{aligned} \tag{A9}$$

and the sphaleron factor is

$$a_{\text{sph}} = \frac{n_{\Delta B}}{n_{\Delta B} - n_{\Delta L}} = \frac{28}{79}, \tag{A10}$$

where

$$\begin{aligned} n_{\Delta B} &= \left(3 \times \frac{1}{3}\right)\frac{T^2}{6}\left[2(\mu_{Q_{L_1}} + \mu_{Q_{L_2}} + \mu_{Q_{L_3}}) + (\mu_{u_{L_1}} + \mu_{u_{L_2}} + \mu_{u_{L_3}}) + (\mu_{d_{R_1}} + \mu_{d_{R_2}} + \mu_{d_{R_3}})\right], \\ n_{\Delta L} &= \frac{T^2}{6}\left[2(\mu_{\ell_{L_1}} + \mu_{\ell_{L_2}} + \mu_{\ell_{L_3}}) + (\mu_{\ell_{R_1}} + \mu_{\ell_{R_2}} + \mu_{\ell_{R_3}})\right]. \end{aligned} \tag{A11}$$

Now, we define $n_{\Delta_\alpha} \equiv \frac{n_{\Delta B}}{3} - n_{\Delta L_\alpha}$ where $n_{\Delta L_\alpha} = T^2(2\mu_{\ell_{L_\alpha}} + \mu_{\ell_{R_\alpha}})/6$ and $\alpha = 1\ldots3$. Using Eq. (A9), we can write

$$n_{\Delta_\alpha} = \frac{T^2}{6}\mathcal{B}_{\alpha\beta}\mu_{\ell_{L_\beta}} = \frac{\mathcal{B}_{\alpha\beta}}{2}n_{\Delta\ell_{L_\beta}}, \tag{A12}$$

and in the last step, we use Eq. (A1). Dividing both sides by the entropy density s gives $Y_{\Delta_\alpha} = \mathcal{P}_{\alpha\beta}Y_{\Delta\ell_{L_\beta}}$ where $P_{\alpha\beta} = \mathcal{B}_{\alpha\beta}/2$. The explicit form of $\mathcal{P}$ is

$$\frac{1}{106}\begin{pmatrix} -205 & -8 & -8 \\ -8 & -205 & -8 \\ -8 & -8 & -205. \end{pmatrix}. \tag{A13}$$

The $\mathcal{A}$ matrix is defined in Eq. (14) as $-\mathcal{P}^{-1}$, and it is given by

$$\frac{1}{711}\begin{pmatrix} 442 & -32 & -32 \\ -32 & 442 & -32 \\ -32 & -32 & 442 \end{pmatrix}. \tag{A14}$$

APPENDIX B: RELEVANT CROSS SECTIONS FOR LEPTOGENISIS

In this section, the analytical form of the cross section is provided in terms of $x \equiv \hat{s}/M_1^2$ where $\hat{s}$ is the Mandelstam variable $r_{\rm BL} = m_{Z_{\rm BL}}/M_1$, and $r_\eta = m_\eta/M_1$.

(1) $N_iN_i \to \bar{f}f$:

$$\sigma_{N_iN_i\to\bar{f}f} = \frac{g_{\rm BL}^4 {\rm Q}_{\rm BL}^{(f)2}}{3\pi M_1^2}\frac{\sqrt{x(x-4)}}{(x-r_{\rm BL}^2)^2 + r_{\rm BL}^2(\Gamma_{Z_{\rm BL}}/M_1)^2}. \tag{B1}$$

(2) $N_iN_i \to \eta\eta$:

$$\sigma_{N_iN_i\to\eta\eta} = 36\lambda_\phi^2 v_{\rm BL}^2 Y_i^2 T^{ss}_{N_iN_i\to\eta\eta} + Y_i^4(T^{tt}_{N_iN_i\to\eta\eta} + T^{uu}_{N_iN_i\to\eta\eta}) + 6\lambda_\phi v_{\rm BL} Y_i^3(T^{ts}_{N_iN_i\to\eta\eta} + T^{us}_{N_iN_i\to\eta\eta}) + Y_i^4 T^{tu}_{N_iN_i\to\eta\eta}, \tag{B2}$$

where

$$T^{ss}_{N_iN_i\to\eta\eta} = \frac{\sqrt{x-4}\sqrt{x-4r_\eta^2}}{8\pi M_1^4 x(r_\eta^2-x)^2}, \tag{B3}$$

$$T^{tt}_{N_iN_i\to\eta\eta} = \frac{(2r_\eta^2 - x - 8)\log\left(\frac{-\sqrt{x-4}\sqrt{x-4r_\eta^2}-2r_\eta^2+x}{\sqrt{x-4}\sqrt{x-4r_\eta^2}-2r_\eta^2+x}\right) - \frac{\sqrt{x-4}\sqrt{x-4r_\eta^2}(2(r_\eta^4-6r_\eta^2+8)+x)}{r_\eta^4-4r_\eta^2+x}}{8\pi M_1^2 x(x-4)}, \tag{B4}$$

$$T^{uu}_{N_iN_i\to\eta\eta} = \frac{(2r_\eta^2 - x - 8)\log\left(\frac{-\sqrt{x-4}\sqrt{x-4r_\eta^2}-2r_\eta^2+x}{\sqrt{x-4}\sqrt{x-4r_\eta^2}-2r_\eta^2+x}\right) - \frac{\sqrt{x-4}\sqrt{x-4r_\eta^2}(2(r_\eta^4-6r_\eta^2+8)+x)}{r_\eta^4-4r_\eta^2+x}}{8\pi M_1^2 x(x-4)}, \tag{B5}$$

$$T^{su}_{N_iN_i\to\eta\eta} = \frac{(2r_\eta^2 + x - 8)\log\left(\frac{-\sqrt{x-4}\sqrt{x-4r_\eta^2}-2r_\eta^2+x}{\sqrt{x-4}\sqrt{x-4r_\eta^2}-2r_\eta^2+x}\right) - 2\sqrt{x-4}\sqrt{x-4r_\eta^2}}{4\pi M_1^3 x(x-4)x(x-r_\eta^2)}, \tag{B6}$$

$$T^{st}_{N_iN_i\to\eta\eta}=\frac{(2r_\eta^2+x-8)\log\left(\frac{-\sqrt{x-4}\sqrt{x-4r_\eta^2}-2r_\eta^2+x}{\sqrt{x-4}\sqrt{x-4r_\eta^2}-2r_\eta^2+x}\right)-2\sqrt{x-4}\sqrt{x-4r_\eta^2}}{4\pi M_1^3x(x-4)(x-r_\eta^2)}, \tag{B7}$$

$$T^{ut}_{N_iN_i\to\eta\eta}=\frac{(r_\eta^4+4(x-4))\log\left(\left(\frac{\sqrt{x-4}\sqrt{x-4r_\eta^2}-2r_\eta^2+x}{\sqrt{x-4}\sqrt{x-4r_\eta^2}+2r_\eta^2-x}\right)^2\right)-\sqrt{x-4}\sqrt{x-4r_\eta^2}(x-2r_\eta^2)}{4\pi M_1^2(x-4)x(x-2r_\eta^2)}. \tag{B8}$$

(3) $N_iN_i\to Z_{\rm BL}Z_{\rm BL}$:

$$\sigma_{N_iN_i\to Z_{\rm BL}Z_{\rm BL}}=g_{\rm BL}^4\left(T^{tt}_{N_iN_i\to Z_{\rm BL}Z_{\rm BL}}+T^{uu}_{N_iN_i\to Z_{\rm BL}Z_{\rm BL}}+T^{ut}_{N_iN_i\to Z_{\rm BL}Z_{\rm BL}}\right)+64g_{\rm BL}^4v_{\rm BL}^2Y_i^2T^{ss}_{N_iN_i\to Z_{\rm BL}Z_{\rm BL}}+8g_{\rm BL}^4v_{\rm BL}Y_i\left(T^{st}_{N_iN_i\to Z_{\rm BL}Z_{\rm BL}}+T^{su}_{N_iN_i\to Z_{\rm BL}Z_{\rm BL}}\right), \tag{B9}$$

where

$$T^{tt}_{N_iN_i\to Z_{\rm BL}Z_{\rm BL}}=\frac{1}{48\pi M_1^2x}\left[\frac{\sqrt{x-4r_{\rm BL}^2}(-48r_{\rm BL}^8+4r_{\rm BL}^6(5x+46)+r_{\rm BL}^4((x-102)x+32))}{r_{\rm BL}^4\sqrt{x-4}(r_{\rm BL}^4-4r_{\rm BL}^2+x)}+\frac{\sqrt{x-4r_{\rm BL}^2}(16r_{\rm BL}^2(x-7)x+x^2(x+2))}{r_{\rm BL}^4\sqrt{x-4}(r_{\rm BL}^4-4r_{\rm BL}^2+x)}-\frac{24(-2r_{\rm BL}^2+x+8)\log\left(\frac{-\sqrt{x-4}\sqrt{x-4r_{\rm BL}^2}-2r_{\rm BL}^2+x}{\sqrt{x-4}\sqrt{x-4r_{\rm BL}^2}-2r_{\rm BL}^2+x}\right)}{x-4}\right],$$

$$T^{uu}_{N_iN_i\to Z_{\rm BL}Z_{\rm BL}}=\frac{1}{48\pi M_1^2x}=\frac{1}{48\pi M_1^2x}\left[\frac{\sqrt{x-4r_{\rm BL}^2}(-48r_{\rm BL}^8+4r_{\rm BL}^6(5x+46)+r_{\rm BL}^4((x-102)x+32))}{r_{\rm BL}^4\sqrt{x-4}(r_{\rm BL}^4-4r_{\rm BL}^2+x)}+\frac{\sqrt{x-4r_{\rm BL}^2}(16r_{\rm BL}^2(x-7)x+x^2(x+2))}{r_{\rm BL}^4\sqrt{x-4}(r_{\rm BL}^4-4r_{\rm BL}^2+x)}-\frac{24(-2r_{\rm BL}^2+x+8)\log\left(\frac{-\sqrt{x-4}\sqrt{x-4r_{\rm BL}^2}-2r_{\rm BL}^2+x}{\sqrt{x-4}\sqrt{x-4r_{\rm BL}^2}-2r_{\rm BL}^2+x}\right)}{x-4}\right],$$

$$T^{ut}_{N_iN_i\to Z_{\rm BL}Z_{\rm BL}}=-\frac{\frac{(4r_{\rm BL}^2(5x+22)+(x-46)x)\sqrt{x-4r_{\rm BL}^2}}{\sqrt{x-4}x}+\frac{48(r_{\rm BL}^2-1)(r_{\rm BL}^4-4r_{\rm BL}^2+x)\log\left(\frac{(\sqrt{x-4}\sqrt{x-4r_{\rm BL}^2}-2r_{\rm BL}^2+x)^2}{(\sqrt{x-4}\sqrt{x-4r_{\rm BL}^2}+2r_{\rm BL}^2-x)^2}\right)}{(x-4)(2r_{\rm BL}^2-x)}}{24\pi M_1^2r_{\rm BL}^4},$$

$$T^{ss}_{N_iN_i\to Z_{\rm BL}Z_{\rm BL}}=\frac{\sqrt{x-4}\sqrt{x-4r_{\rm BL}^2}(12r_{\rm BL}^4-4r_{\rm BL}^2x+x^2)}{32\pi M_1^4r_{\rm BL}^4x(x-r_\eta^2)^2},$$

$$T^{st}_{N_iN_i\to Z_{\rm BL}Z_{\rm BL}}=\frac{1}{4\pi{\rm M}1^3r_{\rm BL}^4(x-4)x(x-r_\eta^2)}\left[-\sqrt{x-4}\sqrt{x-4r_{\rm BL}^2}(4r_{\rm BL}^4-2r_{\rm BL}^2x+x^2)+2(2r_{\rm BL}^6-8r_{\rm BL}^4+4r_{\rm BL}^2x-x^2)\log\left(\frac{-\sqrt{x-4}\sqrt{x-4r_{\rm BL}^2}-2r_{\rm BL}^2+x}{\sqrt{x-4}\sqrt{x-4r_{\rm BL}^2}-2r_{\rm BL}^2+x}\right)\right],$$

$$T^{su}_{N_iN_i\to Z_{\rm BL}Z_{\rm BL}}=\frac{1}{4\pi M_1^3r_{\rm BL}^4(x-4)x(x-r_\eta^2)}\left[-\sqrt{x-4}\sqrt{x-4r_{\rm BL}^2}(4r_{\rm BL}^4-2r_{\rm BL}^2x+x^2)+2(2r_{\rm BL}^6-8r_{\rm BL}^4+4r_{\rm BL}^2x-x^2)\log\left(\frac{-\sqrt{x-4}\sqrt{x-4r_{\rm BL}^2}-2r_{\rm BL}^2+x}{\sqrt{x-4}\sqrt{x-4r_{\rm BL}^2}-2r_{\rm BL}^2+x}\right)\right]. \tag{B10}$$

(4) $N_iN_i \to \eta Z_{\rm BL}$:

$$\sigma_{N_iN_i\to\eta Z_{\rm BL}} = g_{\rm BL}^2 Y_i^2\left(T^{tt}_{N_iN_i\to\eta Z_{\rm BL}} + T^{tt}_{N_iN_i\to\eta Z_{\rm BL}} T^{ut}_{N_iN_i\to\eta Z_{\rm BL}}\right) + 64 g_{\rm BL}^6 v_{\rm BL}^2 T^{ss}_{N_iN_i\to\eta Z_{\rm BL}} + 8 g_{\rm BL}^4 Y_i v_{\rm BL}\left(T^{st}_{N_iN_i\to\eta Z_{\rm BL}} + T^{su}_{N_iN_i\to\eta Z_{\rm BL}}\right), \tag{B11}$$

where

$$T^{tt}_{N_iN_i\to\eta Z_{\rm BL}} = \frac{1}{16\pi M_1^2 x(x-4)}\left[4(r_{\rm BL}^2 + r_\eta^2 - x - 8)\log\left(-\frac{\sqrt{x-4}\sqrt{\frac{(r_{\rm BL}^2-r_\eta^2)^2}{x} - 2(r_{\rm BL}^2+r_\eta^2)+x} + r_{\rm BL}^2 + r_\eta^2 - x}{\sqrt{x-4}\sqrt{\frac{(r_{\rm BL}^2-r_\eta^2)^2}{x} - 2(r_{\rm BL}^2+r_\eta^2)+x} - r_{\rm BL}^2 - r_\eta^2 + x}\right)\right.$$
$$+ \frac{2\sqrt{x-4}\sqrt{\frac{r_{\rm BL}^4 - 2r_{\rm BL}^2(r_\eta^2+x)+(r_\eta^2-x)^2}{x}}(-2r_{\rm BL}^6 + r_{\rm BL}^4(-4r_\eta^2(x-1)+13x-4) - r_{\rm BL}^2(r_\eta^2-4)(2r_\eta^2 - x(x+6)))}{r_{\rm BL}^2(r_{\rm BL}^4 + r_{\rm BL}^2(r_\eta^2(x-2)-2x) + (r_\eta^2-x)^2)}$$
$$\left. + \frac{2\sqrt{x-4}\sqrt{\frac{r_{\rm BL}^4 - 2r_{\rm BL}^2(r_\eta^2+x)+(r_\eta^2-x)^2}{x}}((x-4)(r_\eta^2-x)^2)}{r_{\rm BL}^2(r_{\rm BL}^4 + r_{\rm BL}^2(r_\eta^2(x-2)-2x) + (r_\eta^2-x)^2)}\right], \tag{B12}$$

$$T^{uu}_{N_iN_i\to\eta Z_{\rm BL}} = \frac{1}{16\pi M_1^2 x(x-4)}\left[4(r_{\rm BL}^2 + r_\eta^2 - x - 8)\log\left(-\frac{\sqrt{x-4}\sqrt{\frac{(r_{\rm BL}^2-r_\eta^2)^2}{x} - 2(r_{\rm BL}^2+r_\eta^2)+x} + r_{\rm BL}^2 + r_\eta^2 - x}{\sqrt{x-4}\sqrt{\frac{(r_{\rm BL}^2-r_\eta^2)^2}{x} - 2(r_{\rm BL}^2+r_\eta^2)+x} - r_{\rm BL}^2 - r_\eta^2 + x}\right)\right.$$
$$+ \frac{2\sqrt{x-4}\sqrt{\frac{r_{\rm BL}^4 - 2r_{\rm BL}^2(r_\eta^2+x)+(r_\eta^2-x)^2}{x}}(-2r_{\rm BL}^6 + r_{\rm BL}^4(-4r_\eta^2(x-1)+13x-4) - r_{\rm BL}^2(r_\eta^2-4)(2r_\eta^2 - x(x+6)))}{r_{\rm BL}^2(r_{\rm BL}^4 + r_{\rm BL}^2(r_\eta^2(x-2)-2x) + (r_\eta^2-x)^2)}$$
$$\left. + \frac{2\sqrt{x-4}\sqrt{\frac{r_{\rm BL}^4 - 2r_{\rm BL}^2(r_\eta^2+x)+(r_\eta^2-x)^2}{x}}((x-4)(r_\eta^2-x)^2)}{r_{\rm BL}^2(r_{\rm BL}^4 + r_{\rm BL}^2(r_\eta^2(x-2)-2x) + (r_\eta^2-x)^2)}\right], \tag{B13}$$

$$T^{ut}_{N_iN_i\to\eta Z_{\rm BL}} = \frac{1}{4\pi M_1^2 r_{\rm BL}^2(x-4)x(r_{\rm BL}^2 + r_\eta^2 - x)}\left[-\sqrt{x-4}(-2r_{\rm BL}^2 + x + 4)(-r_{\rm BL}^2 - r_\eta^2 + x)\right.$$
$$\times\sqrt{\frac{r_{\rm BL}^4 - 2r_{\rm BL}^2(r_\eta^2+x)+(r_\eta^2-x)^2}{x}} + 2(r_{\rm BL}^4(r_\eta^2-1) + r_{\rm BL}^2(-(r_\eta^2(x-2)) + 6x - 16) - (r_\eta^2-x)^2)$$
$$\left.\times\log\left(\frac{(\sqrt{x-4}\sqrt{\frac{(r_{\rm BL}^2-r_\eta^2)^2}{x} - 2(r_{\rm BL}^2+r_\eta^2)+x} + r_{\rm BL}^2 + r_\eta^2 - x)^2}{(-\sqrt{x-4}\sqrt{\frac{(r_{\rm BL}^2-r_\eta^2)^2}{x} - 2(r_{\rm BL}^2+r_\eta^2)+x} + r_{\rm BL}^2 + r_\eta^2 - x)^2}\right)\right],$$
$$T^{ss}_{N_iN_i\to\eta Z_{\rm BL}} = \frac{\sqrt{\frac{r_{\rm BL}^4 - 2r_{\rm BL}^2(r_\eta^2+x)+(r_\eta^2-x)^2}{x}}}{48\pi x^2 M_1^4 r_{\rm BL}^6(x-r_{\rm BL}^2)^2\sqrt{x-4}}\left[r_{\rm BL}^8(x+2) - 12 r_{\rm BL}^2 x(r_\eta^4 - r_\eta^2 x + 2x^2) + 6x^2(r_\eta^2-x)^2\right.$$
$$\left. - 2r_{\rm BL}^6(r_\eta^2(x+2) + x(32-5x)) + r_{\rm BL}^4(r_\eta^4(x+2) - 2r_\eta^2(x-10)x + x^2(x+32))\right],$$

$$T^{st}_{N_iN_i\to\eta Z_{\rm BL}}=\frac{1}{4\pi M_1^3 r_{\rm BL}^4(x-4)x(r_{\rm BL}^2-x)}\Bigg[\sqrt{x-4}(4r_{\rm BL}^4-x(r_{\rm BL}^2+r_\eta^2)+x^2)$$
$$\times\sqrt{\frac{r_{\rm BL}^4-2r_{\rm BL}^2(r_\eta^2+x)+(r_\eta^2-x)^2}{x}}+2(r_{\rm BL}^6+r_{\rm BL}^4(r_\eta^2+x-9)+r_{\rm BL}^2(2x-r_\eta^2(x-2))-(r_\eta^2-x)^2)$$
$$\times\log\left(\frac{-\sqrt{x-4}\sqrt{\frac{(r_{\rm BL}^2-r_\eta^2)^2}{x}-2(r_{\rm BL}^2+r_\eta^2)+x}+r_{\rm BL}^2+r_\eta^2-x}{\sqrt{x-4}\sqrt{\frac{(r_{\rm BL}^2-r_\eta^2)^2}{x}-2(r_{\rm BL}^2+r_\eta^2)+x}+r_{\rm BL}^2+r_\eta^2-x}\right)\Bigg],$$
$$T^{su}_{N_iN_i\to\eta Z_{\rm BL}}=\frac{1}{4\pi M_1^3 r_{\rm BL}^4(x-4)x(r_{\rm BL}^2-x)}\Bigg[\sqrt{x-4}(4r_{\rm BL}^4-x(r_{\rm BL}^2+r_\eta^2)+x^2)$$
$$\times\sqrt{\frac{r_{\rm BL}^4-2r_{\rm BL}^2(r_\eta^2+x)+(r_\eta^2-x)^2}{x}}-2(r_{\rm BL}^6+r_{\rm BL}^4(r_\eta^2+x-9)+r_{\rm BL}^2(2x-r_\eta^2(x-2))-(r_\eta^2-x)^2)$$
$$\times\log\left(-\frac{\sqrt{x-4}\sqrt{\frac{(r_{\rm BL}^2-r_\eta^2)^2}{x}-2(r_{\rm BL}^2+r_\eta^2)+x}+r_{\rm BL}^2+r_\eta^2-x}{\sqrt{x-4}\sqrt{\frac{(r_{\rm BL}^2-r_\eta^2)^2}{x}-2(r_{\rm BL}^2+r_\eta^2)+x}-r_{\rm BL}^2-r_\eta^2+x}\right)\Bigg]. \tag{B14}$$

(5) $\bar{t}_R U_{3_L}\to\ell_{\alpha_L}N_i$:

$$\sigma_{\bar{t}_R U_{3_L}\to\ell_{\alpha_L}N_i}=|Y_{33}|^2|Y_{{\rm D}\alpha i}|^2\frac{(x-1)^2}{4\pi M_1^2 x^3}. \tag{B15}$$

(6) $\ell_{\alpha_L}t_R\to U_{3_L}N_i$:

$$\sigma_{\ell_{\alpha_L}t_R\to U_{3_L}N_i}=|Y_{33}|^2|Y_{{\rm D}\alpha i}|^2\frac{(x-1)(2\delta^2+x-2)+(2\delta^2-1)(\delta^2+x-1)\log\left(\frac{\delta^2}{\delta^2+x-1}\right)}{4\pi M_1^2 x^2\left(\delta^2+x-1\right)}. \tag{B16}$$

(7) $\overline{\ell}_{\alpha_L}U_{3_L}\to t_R N_i$:

$$\sigma_{\overline{\ell}_{\alpha_L}U_{3_L}\to t_R N_i}=|Y_{33}|^2|Y_{{\rm D}\alpha i}|^2\frac{(x-1)(2\delta^2+x-2)+(2\delta^2-1)(\delta^2+x-1)\log\left(\frac{\delta^2}{\delta^2+x-1}\right)}{4\pi M_1^2 x^2(\delta^2+x-1)}. \tag{B17}$$

In both of the above equations, Y_{33} is the third-generation up-type Yukawa coupling, and we added a regulator mass δM_1 in the t channel propagator, and we consider $\delta=0.1$ throughout our analysis.

APPENDIX C: COLLISION TERMS FOR LEPTON-FLAVOR-VIOLATING PROCESSES

There are four scatterings involving the members of the left-handed lepton doublet and Higgs doublet where the lepton flavor (ℓ_α) is violated. These scatterings and corresponding collision terms are listed below.

(i) $\ell_\alpha H\rightleftharpoons\overline{\ell}_\beta H^\star$

$$\mathcal{C}_{\alpha\beta}=-2s\sum_\beta\langle\sigma'_{\ell_\alpha H\to\overline{\ell}_\beta H^\star}v\rangle Y^{\rm eq}_{\ell_\alpha}Y^{\rm eq}_H\left(\frac{n_{\Delta\ell_\alpha}}{2n^{\rm eq}_\alpha}+\frac{n_{\Delta\ell_\beta}}{2n^{\rm eq}_\beta}\right). \tag{C1}$$

(ii) $\ell_\alpha\ell_\beta\rightleftharpoons H^\star H^\star$

$$\mathcal{C}_{\alpha\beta}=-2s\sum_\beta\langle\sigma_{\ell_\alpha\ell_\beta\to H^\star H^\star}v\rangle Y^{\rm eq}_{\ell_\alpha}Y^{\rm eq}_H\left(\frac{n_{\Delta\ell_\alpha}}{2n^{\rm eq}_\alpha}+\frac{n_{\Delta\ell_\beta}}{2n^{\rm eq}_\beta}\right). \tag{C2}$$

(iii) $\ell_\alpha\overline{\ell_\beta}\rightleftharpoons HH^\star$ $(\alpha\neq\beta)$

$$\mathcal{C}_{\alpha\beta}=-2s\sum_\beta\langle\sigma_{\ell_\alpha\overline{\ell_\beta}\to HH^\star}v\rangle Y^{\rm eq}_{\ell_\alpha}Y^{\rm eq}_H\left(\frac{n_{\Delta\ell_\alpha}}{2n^{\rm eq}_\alpha}-\frac{n_{\Delta\ell_\beta}}{2n^{\rm eq}_\beta}\right). \tag{C3}$$

(iv) $\ell_\alpha H\rightleftharpoons\ell_\beta H$ $(\alpha\neq\beta)$

$$\mathcal{C}_{\alpha\beta}=-2s\sum_\beta\langle\sigma_{\ell_\alpha H\to\ell_\beta H}v\rangle Y^{\rm eq}_{\ell_\alpha}Y^{\rm eq}_H\left(\frac{n_{\Delta\ell_\alpha}}{2n^{\rm eq}_\alpha}-\frac{n_{\Delta\ell_\beta}}{2n^{\rm eq}_\beta}\right). \tag{C4}$$

APPENDIX D: FIELD-DEPENDENT MASSES AND THERMAL MASSES

The field-dependent mass of the scalar fields in the diagonal basis, i.e., in the (ξ,η) basis, is given by

$$\bar{m}^2_\xi=\frac{\bar{m}^2_{\zeta_1}+\bar{m}^2_{\eta_1}+\sqrt{(\bar{m}^2_{\zeta_1}-\bar{m}^2_{\eta_1})^2+4\bar{m}^4_{\zeta_1\eta_1}}}{2},$$
$$\bar{m}^2_\eta=\frac{\bar{m}^2_{\zeta_1}+\bar{m}^2_{\eta_1}-\sqrt{(\bar{m}^2_{\zeta_1}-\bar{m}^2_{\eta_1})^2+4\bar{m}^4_{\zeta_1\eta_1}}}{2}, \tag{D1}$$

where

$$\bar{m}^2_{\zeta_1}=-\mu^2_H+3\lambda_H\zeta_1^2-\frac{\lambda'}{2}\eta_1^2,\quad \bar{m}^2_{\eta_1}=-\mu^2_\Phi+3\lambda_\Phi\eta_1^2-\frac{\lambda'}{2}\zeta_1^2,$$
$$\bar{m}^2_{\zeta_1\eta_1}=-\lambda'\zeta_1\eta_1. \tag{D2}$$

The field-dependent mass of the neutral SM gauge boson is given by

$$\bar{m}^2_Z=\frac{\bar{m}^2_{11}+\bar{m}^2_{22}+\sqrt{(\bar{m}^2_{11}-\bar{m}^2_{22})^2+4\bar{m}^4_{12}}}{2},$$
$$\bar{m}^2_\gamma=\frac{\bar{m}^2_{11}+\bar{m}^2_{22}-\sqrt{(\bar{m}^2_{11}-\bar{m}^2_{22})^2+4\bar{m}^4_{12}}}{2}, \tag{D3}$$

where

$$\bar{m}^2_{11}=\frac{g_2^2\zeta_1^2}{4},\quad \bar{m}^2_{22}=\frac{g_1^2\zeta_1^2}{4},\quad \bar{m}^2_{12}=\frac{-g_1g_2\zeta_1^2}{4}. \tag{D4}$$

The field-dependent mass of the Goldstone modes, W boson, $Z_{\rm BL}$, and fermions are as follows:

$$\bar{m}^2_{G^+}=-\mu^2_H+\lambda_H\zeta_1^2-\frac{\lambda'}{2}\eta_1^2,\quad \bar{m}^2_{\zeta_2}=-\mu^2_H+\lambda_H\zeta_1^2-\frac{\lambda'}{2}\eta_1^2,\quad \bar{m}^2_{\eta_2}=-\mu^2_\Phi+\lambda_\Phi\eta_1^2-\frac{\lambda'}{2}\zeta_1^2,$$
$$\bar{m}^2_W=\left(\frac{m_W}{v_h}\right)^2\zeta_1^2,\quad \bar{m}^2_{Z_{\rm BL}}=\left(\frac{m_{Z_{\rm BL}}}{v_{\rm BL}}\right)^2\eta_1^2,\quad \bar{m}^2_t=\left(\frac{m_t}{v_h}\right)^2\zeta_1^2,\quad \bar{m}^2_i=\left(\frac{M_i}{v_{\rm BL}}\right)^2\eta_1^2. \tag{D5}$$

One can obtain the field-dependent mass of ξ and η in the thermal background by performing the following replacement in Eq. (D2):

$$\bar{m}^2_\zeta\to\bar{m}^2_\zeta+\Pi^2_{\zeta_1},\qquad \bar{m}^2_\eta\to\bar{m}^2_\eta+\Pi^2_{\eta_1}, \tag{D6}$$

where

$$\Pi^2_{\zeta_1}=\left(\frac{g_1^2}{16}+\frac{3g_2^2}{16}+\frac{y_t^2}{4}+\frac{\lambda_H}{2}-\frac{\lambda'}{12}\right)T^2,$$
$$\Pi^2_{\eta_1}=\left(g^2_{\rm BL}+\frac{3g_2^2}{16}+\frac{Y_i}{8}+\frac{\lambda_\Phi}{3}-\frac{\lambda'}{6}\right)T^2. \tag{D7}$$

Similarly, the longitudinal modes of the gauge boson get thermal correction and $\bar{m}^L_{W,T}=\bar{m}_W+11g_2^2T^2/6$. Similar to the scalar case, one can obtain the thermal mass correction to the longitudinal modes of the neutral SM gauge bosons by replacing $\bar{m}^2_{11}\to\bar{m}^2_{11}+11g_2^2T^2/6$ and $\bar{m}^2_{22}\to\bar{m}^2_{22}+11g_1^2T^2/6$ in Eq. (D3). The field-dependent mass of Goldstone modes and longitudinal $Z_{\rm BL}$ in the thermal background is as follows:

$$\bar{m}^2_{G^+,T}=\bar{m}^2_{G^+}+\Pi^2_{\zeta_1},\qquad \bar{m}^2_{\zeta_2,T}=\bar{m}^2_{\zeta_2}+\Pi^2_{\zeta_1},$$
$$\bar{m}^2_{\eta_2,T}=\bar{m}^2_{\eta_2}+\Pi^2_{\eta_1},\qquad \bar{m}^2_{Z_{\rm BL},T}=\bar{m}^2_{Z_{\rm BL}}+4g^2_{\rm BL}T^2. \tag{D8}$$

[1] Y. Fukuda *et al.* (Super-Kamiokande Collaboration), Evidence for oscillation of atmospheric neutrinos, Phys. Rev. Lett. **81**, 1562 (1998).

[2] Q. R. Ahmad *et al.* (SNO Collaboration), Direct evidence for neutrino flavor transformation from neutral current interactions in the Sudbury Neutrino Observatory, Phys. Rev. Lett. **89**, 011301 (2002).

[3] P. Minkowski, $\mu \to e\gamma$ at a rate of one out of 10^9 muon decays?, Phys. Lett. **67B**, 421 (1977).

[4] T. Yanagida, Horizontal gauge symmetry and masses of neutrinos, Conf. Proc. C **7902131**, 95 (1979).

[5] S. Navas *et al.* (Particle Data Group), Review of particle physics, Phys. Rev. D **110**, 030001 (2024).

[6] S. Davidson, E. Nardi, and Y. Nir, Leptogenesis, Phys. Rep. **466**, 105 (2008).

[7] M. Yoshimura, Unified gauge theories and the baryon number of the universe, Phys. Rev. Lett. **41**, 281 (1978); **42**, 746(E) (1979).

[8] J. R. Ellis, M. K. Gaillard, and D. V. Nanopoulos, Baryon number generation in grand unified theories, Phys. Lett. **80B**, 360 (1979); **82B**, 464(E) (1979).

[9] D. V. Nanopoulos and S. Weinberg, Mechanisms for cosmological baryon production, Phys. Rev. D **20**, 2484 (1979).

[10] I. Affleck and M. Dine, A new mechanism for baryogenesis, Nucl. Phys. **B249**, 361 (1985).

[11] M. Dine, L. Randall, and S. D. Thomas, Baryogenesis from flat directions of the supersymmetric standard model, Nucl. Phys. **B458**, 291 (1996).

[12] A. Riotto and M. Trodden, Recent progress in baryogenesis, Annu. Rev. Nucl. Part. Sci. **49**, 35 (1999).

[13] M. Dine and A. Kusenko, The origin of the matter—antimatter asymmetry, Rev. Mod. Phys. **76**, 1 (2003).

[14] J. M. Cline, Baryogenesis, arXiv:hep-ph/0609145.

[15] D. E. Morrissey and M. J. Ramsey-Musolf, Electroweak baryogenesis, New J. Phys. **14**, 125003 (2012).

[16] M. A. Luty, Baryogenesis via leptogenesis, Phys. Rev. D **45**, 455 (1992).

[17] T. Gherghetta and G. Jungman, Cosmological consequences of spontaneous lepton number violation in SO (10) grand unification, Phys. Rev. D **48**, 1546 (1993).

[18] M. Plumacher, Baryogenesis and lepton number violation, Z. Phys. C **74**, 549 (1997).

[19] L. Covi, E. Roulet, and F. Vissani, *CP* violating decays in leptogenesis scenarios, Phys. Lett. B **384**, 169 (1996).

[20] M. Plumacher, Baryon asymmetry, neutrino mixing and supersymmetric SO(10) unification, Nucl. Phys. **B530**, 207 (1998).

[21] M. Plümacher, Baryon asymmetry, neutrino mixing and supersymmetric SO(10) unification, 10.3204/PUBDB-2016-02633 (1998).

[22] W. Buchmuller and M. Plumacher, Matter antimatter asymmetry and neutrino properties, Phys. Rep. **320**, 329 (1999).

[23] W. Buchmuller and M. Plumacher, Neutrino masses and the baryon asymmetry, Int. J. Mod. Phys. A **15**, 5047 (2000).

[24] W. Buchmuller, P. Di Bari, and M. Plumacher, Leptogenesis for pedestrians, Ann. Phys. (Amsterdam) **315**, 305 (2005).

[25] G. F. Giudice, A. Notari, M. Raidal, A. Riotto, and A. Strumia, Towards a complete theory of thermal leptogenesis in the SM and MSSM, Nucl. Phys. **B685**, 89 (2004).

[26] S. Iso, N. Okada, and Y. Orikasa, Resonant leptogenesis in the minimal B-L extended standard model at TeV, Phys. Rev. D **83**, 093011 (2011).

[27] N. Sahu and U. A. Yajnik, Dark matter and leptogenesis in gauged B—L symmetric models embedding nu MSM, Phys. Lett. B **635**, 11 (2006).

[28] C.-Q. Geng and H. Okada, Neutrino masses, dark matter and leptogenesis with $U(1)_{B-L}$ gauge symmetry, Phys. Dark Universe **20**, 13 (2018).

[29] A. Biswas, S. Choubey, and S. Khan, Neutrino mass, leptogenesis and FIMP dark matter in a $U(1)_{B-L}$ model, Eur. Phys. J. C **77**, 875 (2017).

[30] R. Pramanick, T. S. Ray, and A. Shaw, Neutrino mass and leptogenesis in a hybrid seesaw model with a spontaneously broken *CP*, J. High Energy Phys. 06 (2023) 099.

[31] R. Pramanick, T. S. Ray, and A. Sil, Toward a more complete description of hybrid leptogenesis, Phys. Rev. D **109**, 115011 (2024).

[32] A. Das and Y. Orikasa, Resonant leptogenesis in minimal U(1)X extensions of the standard model, Phys. Lett. B **864**, 139395 (2025).

[33] D. Bose, R. Pramanick, and T. S. Ray, Cogenesis of visible and dark matter in a scotogenic model, arXiv:2409.06541.

[34] S. Davidson and A. Ibarra, A lower bound on the right-handed neutrino mass from leptogenesis, Phys. Lett. B **535**, 25 (2002).

[35] A. Abada, S. Davidson, A. Ibarra, F. X. Josse-Michaux, M. Losada, and A. Riotto, Flavour matters in leptogenesis, J. High Energy Phys. 09 (2006) 010.

[36] E. Nardi, Y. Nir, E. Roulet, and J. Racker, The importance of flavor in leptogenesis, J. High Energy Phys. 01 (2006) 164.

[37] S. Blanchet and P. Di Bari, Flavor effects on leptogenesis predictions, J. Cosmol. Astropart. Phys. 03 (2007) 018.

[38] B. Adhikary, M. Chakraborty, and A. Ghosal, Flavored leptogenesis with quasidegenerate neutrinos in a broken cyclic symmetric model, Phys. Rev. D **93**, 113001 (2016).

[39] D. Aristizabal Sierra, M. Dhen, and T. Hambye, Scalar triplet flavored leptogenesis: A systematic approach, J. Cosmol. Astropart. Phys. 08 (2014) 003.

[40] P. S. B. Dev, P. Di Bari, B. Garbrecht, S. Lavignac, P. Millington, and D. Teresi, Flavor effects in leptogenesis, Int. J. Mod. Phys. A **33**, 1842001 (2018).

[41] A. Vilenkin, Gravitational radiation from cosmic strings, Phys. Lett. **107B**, 47 (1981).

[42] T. Vachaspati and A. Vilenkin, Gravitational radiation from cosmic strings, Phys. Rev. D **31**, 3052 (1985).

[43] T. Damour and A. Vilenkin, Gravitational radiation from cosmic (super)strings: Bursts, stochastic background, and observational windows, Phys. Rev. D **71**, 063510 (2005).

[44] K. Schmitz, New sensitivity curves for gravitational-wave signals from cosmological phase transitions, J. High Energy Phys. 01 (2021) 097.

[45] L. P. Grishchuk, Amplification of gravitational waves in an isotropic universe, Zh. Eksp. Teor. Fiz. **67**, 825 (1974).

[46] L. P. Grishchuk, Quantum effects in cosmology, Classical Quantum Gravity **10**, 2449 (1993).
[47] E. Witten, Cosmic separation of phases, Phys. Rev. D **30**, 272 (1984).
[48] M. Kamionkowski, A. Kosowsky, and M. S. Turner, Gravitational radiation from first order phase transitions, Phys. Rev. D **49**, 2837 (1994).
[49] M. Maggiore, Gravitational wave experiments and early universe cosmology, Phys. Rep. **331**, 283 (2000).
[50] J. M. Cline and P.-A. Lemieux, Electroweak phase transition in two Higgs doublet models, Phys. Rev. D **55**, 3873 (1997).
[51] S. Profumo, M. J. Ramsey-Musolf, and G. Shaughnessy, Singlet Higgs phenomenology and the electroweak phase transition, J. High Energy Phys. 08 (2007) 010.
[52] V. Barger, P. Langacker, M. McCaskey, M. Ramsey-Musolf, and G. Shaughnessy, Complex singlet extension of the standard model, Phys. Rev. D **79**, 015018 (2009).
[53] P. Fileviez Perez, H. H. Patel, M. J. Ramsey-Musolf, and K. Wang, Triplet scalars and dark matter at the LHC, Phys. Rev. D **79**, 055024 (2009).
[54] M. Gonderinger, Y. Li, H. Patel, and M. J. Ramsey-Musolf, Vacuum stability, perturbativity, and scalar singlet dark matter, J. High Energy Phys. 01 (2010) 053.
[55] H. H. Patel and M. J. Ramsey-Musolf, Baryon washout, electroweak phase transition, and perturbation theory, J. High Energy Phys. 07 (2011) 029.
[56] S. Profumo, M. J. Ramsey-Musolf, C. L. Wainwright, and P. Winslow, Singlet-catalyzed electroweak phase transitions and precision Higgs boson studies, Phys. Rev. D **91**, 035018 (2015).
[57] A. Beniwal, M. Lewicki, J. D. Wells, M. White, and A. G. Williams, Gravitational wave, collider and dark matter signals from a scalar singlet electroweak baryogenesis, J. High Energy Phys. 08 (2017) 108.
[58] A. Beniwal, M. Lewicki, M. White, and A. G. Williams, Gravitational waves and electroweak baryogenesis in a global study of the extended scalar singlet model, J. High Energy Phys. 02 (2019) 183.
[59] L. Niemi, H. H. Patel, M. J. Ramsey-Musolf, T. V. I. Tenkanen, and D. J. Weir, Electroweak phase transition in the real triplet extension of the SM: Dimensional reduction, Phys. Rev. D **100**, 035002 (2019).
[60] M. J. Ramsey-Musolf, The electroweak phase transition: A collider target, J. High Energy Phys. 09 (2020) 179.
[61] K. Hashino, M. Kakizaki, S. Kanemura, P. Ko, and T. Matsui, Gravitational waves from first order electroweak phase transition in models with the $U(1)_X$ gauge symmetry, J. High Energy Phys. 06 (2018) 088.
[62] J. Kozaczuk, M. J. Ramsey-Musolf, and J. Shelton, Exotic Higgs boson decays and the electroweak phase transition, Phys. Rev. D **101**, 115035 (2020).
[63] L. Niemi, M. J. Ramsey-Musolf, T. V. I. Tenkanen, and D. J. Weir, Thermodynamics of a two-step electroweak phase transition, Phys. Rev. Lett. **126**, 171802 (2021).
[64] C.-W. Chiang, G. Cottin, Y. Du, K. Fuyuto, and M. J. Ramsey-Musolf, Collider probes of real triplet scalar dark matter, J. High Energy Phys. 01 (2021) 198.
[65] J. M. Cline, B. Laurent, S. Raby, and J.-S. Roux, PeV-scale leptogenesis, gravitational waves, and black holes from a SUSY-breaking phase transition, Phys. Rev. D **107**, 095011 (2023).
[66] J. Ellis, M. Lewicki, M. Merchand, J. M. No, and M. Zych, The scalar singlet extension of the standard model: Gravitational waves versus baryogenesis, J. High Energy Phys. 01 (2023) 093.
[67] A. Chatterjee, A. Datta, and S. Roy, Electroweak phase transition in the Z_3-invariant NMSSM: Implications of LHC and dark matter searches and prospects of detecting the gravitational waves, J. High Energy Phys. 06 (2022) 108.
[68] P. Ghosh, T. Ghosh, and S. Roy, Interplay among gravitational waves, dark matter and collider signals in the singlet scalar extended type-II seesaw model, J. High Energy Phys. 10 (2023) 057.
[69] F. Costa, S. Khan, and J. Kim, A two-component vector WIMP—fermion FIMP dark matter model with an extended seesaw mechanism, J. High Energy Phys. 12 (2022) 165.
[70] P. Borah, P. Ghosh, S. Roy, and A. K. Saha, Electroweak phase transition in a right-handed neutrino superfield extended NMSSM, J. High Energy Phys. 08 (2023) 029.
[71] P. Borah, P. Ghosh, and A. K. Saha, Prospecting bipartite dark matter through gravitational waves, J. Cosmol. Astropart. Phys. 05 (2025) 035.
[72] J. Kersten, S. C. Park, Y. Park, J. Son, and L. Velasco-Sevilla, Gravitational waves from a first-order phase transition of the inflaton, J. Cosmol. Astropart. Phys. 04 (2025) 053.
[73] S. Yaser Ayazi, M. Hosseini, and R. Rouzbehi, Gravitational wave signatures of first-order phase transition in two-component dark matter model, Phys. Rev. D **110**, 115027 (2024).
[74] S. Jangid, A. Biswas, and S. C. Park, Strongly electroweak phase transition with $U(1)_{L_\mu - L_\tau}$ gauged non-zero hypercharge triplet, Prog. Theor. Exp. Phys. **2026**, ptag014 (2026).
[75] S. Mahapatra, P. K. Paul, N. Sahu, and P. Shukla, Verifiable type-III seesaw and dark matter in a gauged $U(1)_{\mathrm{B-L}}$ symmetric model, Eur. Phys. J. C **86**, 67 (2026).
[76] P. Bittar, S. Roy, and C. E. M. Wagner, Self consistent thermal resummation: A case study of the phase transition in 2HDM, J. High Energy Phys. 12 (2025) 021.
[77] M. J. Baker, J. Kopp, and A. J. Long, Filtered dark matter at a first order phase transition, Phys. Rev. Lett. **125**, 151102 (2020).
[78] D. Chway, T. H. Jung, and C. S. Shin, Dark matter filtering-out effect during a first-order phase transition, Phys. Rev. D **101**, 095019 (2020).
[79] T. H. Jung and T. Okui, Primordial black holes from bubble collisions during a first-order phase transition, Phys. Rev. D **110**, 115014 (2024).
[80] P. Huang and K.-P. Xie, Leptogenesis triggered by a first-order phase transition, J. High Energy Phys. 09 (2022) 052.
[81] A. Dasgupta, P. S. B. Dev, A. Ghoshal, and A. Mazumdar, Gravitational wave pathway to testable leptogenesis, Phys. Rev. D **106**, 075027 (2022).
[82] E. J. Chun, T. P. Dutka, T. H. Jung, X. Nagels, and M. Vanvlasselaer, Bubble-assisted leptogenesis, J. High Energy Phys. 09 (2023) 164.

[83] Y. Gouttenoire and T. Volansky, Primordial black holes from supercooled phase transitions, Phys. Rev. D **110**, 043514 (2024).

[84] W.-Y. Ai, L. Heurtier, and T. H. Jung, Primordial black holes from an interrupted phase transition, Phys. Rev. D **113**, 023542 (2026).

[85] T. P. Dutka, T. H. Jung, and C. S. Shin, What happens when supercooling is terminated by curvature flipping of the effective potential?, J. High Energy Phys. 05 (2025) 182.

[86] D. Bhandari and A. Sil, Exploring leptogenesis in the era of first order electroweak phase transition, arXiv:2504.03837.

[87] K. Murai, K. Sakurai, and F. Takahashi, Primordial black hole formation via inverted bubble collapse, J. High Energy Phys. 07 (2025) 065.

[88] N. Okada and O. Seto, Probing the seesaw scale with gravitational waves, Phys. Rev. D **98**, 063532 (2018).

[89] T. Hasegawa, N. Okada, and O. Seto, Gravitational waves from the minimal gauged $U(1)_{B-L}$ model, Phys. Rev. D **99**, 095039 (2019).

[90] M. Dichtl, J. Nava, S. Pascoli, and F. Sala, Baryogenesis and leptogenesis from supercooled confinement, J. High Energy Phys. 02 (2024) 059.

[91] A. Datta and A. Sil, Probing leptogenesis through gravitational waves, arXiv:2410.01900.

[92] P. K. Paul, N. Sahu, and P. Shukla, Thermal leptogenesis, dark matter and gravitational waves from an extended canonical seesaw, Phys. Rev. D **112**, 015032 (2025).

[93] B. Barman, A. Das, S. Jyoti Das, and M. Merchand, Hunting for heavy Z' with IceCube neutrinos and gravitational waves, Phys. Rev. D **112**, 035035 (2025).

[94] J. Baker *et al.*, The laser interferometer space antenna: Unveiling the millihertz gravitational wave sky, arXiv:1907.06482.

[95] V. Corbin and N. J. Cornish, Detecting the cosmic gravitational wave background with the big bang observer, Classical Quantum Gravity **23**, 2435 (2006).

[96] J. Crowder and N. J. Cornish, Beyond LISA: Exploring future gravitational wave missions, Phys. Rev. D **72**, 083005 (2005).

[97] G. M. Harry, P. Fritschel, D. A. Shaddock, W. Folkner, and E. S. Phinney, Laser interferometry for the big bang observer, Classical Quantum Gravity **23**, 4887 (2006); **23**, 7361(E) (2006).

[98] N. Seto, S. Kawamura, and T. Nakamura, Possibility of direct measurement of the acceleration of the universe using 0.1-Hz band laser interferometer gravitational wave antenna in space, Phys. Rev. Lett. **87**, 221103 (2001).

[99] S. Kawamura *et al.*, The Japanese space gravitational wave antenna DECIGO, Classical Quantum Gravity **23**, S125 (2006).

[100] S. Kawamura *et al.*, Current status of space gravitational wave antenna DECIGO and B-DECIGO, Prog. Theor. Exp. Phys. **2021**, 05A105 (2021).

[101] J. A. Casas and A. Ibarra, Oscillating neutrinos and $\mu \to e, \gamma$, Nucl. Phys. **B618**, 171 (2001).

[102] A. Granelli, K. Moffat, and S. T. Petcov, Flavoured resonant leptogenesis at sub-TeV scales, Nucl. Phys. **B973**, 115597 (2021).

[103] M. E. Peskin and T. Takeuchi, Estimation of oblique electroweak corrections, Phys. Rev. D **46**, 381 (1992).

[104] S. Baek, P. Ko, and W.-I. Park, Search for the Higgs portal to a singlet fermionic dark matter at the LHC, J. High Energy Phys. 02 (2012) 047.

[105] J. Ellis and T. You, Updated global analysis of Higgs couplings, J. High Energy Phys. 06 (2013) 103.

[106] T. Li and Y.-F. Zhou, Strongly first order phase transition in the singlet fermionic dark matter model after LUX, J. High Energy Phys. 07 (2014) 006.

[107] M. Escudero, S. J. Witte, and N. Rius, The dispirited case of gauged $U(1)_{B-L}$ dark matter, J. High Energy Phys. 08 (2018) 190.

[108] P. Fileviez Pérez and A. D. Plascencia, Probing the nature of neutrinos with a new force, Phys. Rev. D **102**, 015010 (2020).

[109] P. S. B. Dev, A. Pilaftsis, and U.-k. Yang, New production mechanism for heavy neutrinos at the LHC, Phys. Rev. Lett. **112**, 081801 (2014).

[110] F. F. Deppisch, P. S. Bhupal Dev, and A. Pilaftsis, Neutrinos and collider physics, New J. Phys. **17**, 075019 (2015).

[111] D. A. Jones, A fuller flavour treatment of leptogenesis, Ph.D. thesis, Southampton University, 2013.

[112] S. R. Coleman and E. J. Weinberg, Radiative corrections as the origin of spontaneous symmetry breaking, Phys. Rev. D **7**, 1888 (1973).

[113] R. Fukuda and T. Kugo, Gauge invariance in the effective action and potential, Phys. Rev. D **13**, 3469 (1976).

[114] N. K. Nielsen, On the gauge dependence of spontaneous symmetry breaking in gauge theories, Nucl. Phys. **B101**, 173 (1975).

[115] C. Delaunay, C. Grojean, and J. D. Wells, Dynamics of non-renormalizable electroweak symmetry breaking, J. High Energy Phys. 04 (2008) 029.

[116] W. H. Press, S. A. Teukolsky, W. T. Vetterling, and B. P. Flannery, *Numerical Recipes in FORTRAN: The Art of Scientific Computing* (Cambridge University Press, 1992).

[117] M. Quiros, Finite temperature field theory and phase transitions, arXiv:hep-ph/9901312.

[118] P. B. Arnold and O. Espinosa, The effective potential and first order phase transitions: Beyond leading-order, Phys. Rev. D **47**, 3546 (1993); **50**, 6662(E) (1994).

[119] C. Caprini *et al.*, Science with the space-based interferometer eLISA. II: Gravitational waves from cosmological phase transitions, J. Cosmol. Astropart. Phys. 04 (2016) 001.

[120] B. Laurent and J. M. Cline, First principles determination of bubble wall velocity, Phys. Rev. D **106**, 023501 (2022).

[121] T. Krajewski, M. Lewicki, and M. Zych, Bubble-wall velocity in local thermal equilibrium: Hydrodynamical simulations vs analytical treatment, J. High Energy Phys. 05 (2024) 011.

[122] Y. Gouttenoire, R. Jinno, and F. Sala, Friction pressure on relativistic bubble walls, J. High Energy Phys. 05 (2022) 004.

[123] J. Ellis, M. Lewicki, and J. M. No, On the maximal strength of a first-order electroweak phase transition and its gravitational wave signal, J. Cosmol. Astropart. Phys. 04 (2019) 003.

[124] A. D. Linde, Decay of the false vacuum at finite temperature, Nucl. Phys. **B216**, 421 (1983); **B223**, 544 (E) (1983).

[125] C. L. Wainwright, CosmoTransitions: Computing cosmological phase transition temperatures and bubble profiles with multiple fields, Comput. Phys. Commun. **183**, 2006 (2012).

[126] A. Ringwald, K. Saikawa, and C. Tamarit, Primordial gravitational waves in a minimal model of particle physics and cosmology, J. Cosmol. Astropart. Phys. 02 (2021) 046.